Taylor vortex flow under harmonic modulation of the driving force

H. Kuhlmann, D. Roth, and M. Lücke

Institut für Theoretische Physik, Universität des Saarlandes, D-6600 Saarbrücken, West Germany

(Received 30 March 1988; revised manuscript received 26 August 1988)

Time-periodic Taylor vortex flow between two concentric cylinders is studied. With the outer cylinder at rest and the inner one rotating with angular velocity $\Omega(t) = \Omega(1 + \Delta\cos\omega t)$, the stability boundary of circular Couette flow and the fully nonlinear Taylor vortices are investigated. Results are obtained by a finite-difference numerical simulation of the full Navier-Stokes equations for a radius ratio $\eta = 0.65$ and by an analytical Galerkin approximation with four modes for arbitrary gap width. Data obtained by both methods agree very well. Modulation is found to destabilize the basic flow in agreement with earlier theoretical results. The time dependence of Taylor vortices is determined in detail and compared with recent experiments. Their response to the modulated driving is elucidated and explained by investigating various limiting behaviors and by comparison with the amplitude equation. Subharmonic response is found for large modulation amplitudes when the driving $\Omega(t)$ becomes supercritical in both rotation directions during one period. Differences and similarities of linear and nonlinear flow properties with modulated convection in Rayleigh-Bénard systems are discussed in detail. That low-frequency small-amplitude modulation stabilizes the basic conductive state in the latter system while it destabilizes circular Couette flow is shown to be caused by the different coupling of the driving to the secondary flow field.

I. INTRODUCTION

The flow of an incompressible fluid between two concentric cylinders is investigated. While the outer cylinder is held at rest, the inner one is driving the flow by either a uniform rotation with constant angular velocity Ω or by a harmonically modulated rotation rate $\Omega(t)$ with mean Ω. In both cases the primary purely azimuthal circular Couette flow (CCF) state loses its stability to the secondary axisymmetric Taylor vortex flow (TVF) state if the mean angular speed of the inner cylinder exceeds a critical value. For stationary driving both CCF and TVF are time independent whereas for a harmonically modulated driving CCF and TVF are periodic in time. The spatial properties of CCF and TVF, however, remain largely unaffected by the modulation.

The influence of harmonic modulation of the control parameter on hydrodynamic instabilities and secondary flows is of general interest. Especially modulated CCF and TVF had received much attention after the early stimulating work of Donelly.[1] Since that time most investigators aimed at determining the modulation-induced shift of the stability boundary of CCF (Ref. 1–9). Hall[2] used an expansion in terms of a small modulation amplitude and calculated the lowest-order corrections to the threshold shift analytically within a narrow-gap approximation. He found the shift in the threshold for onset of TVF to be negative and small in size for all modulation frequencies being strongest for low-frequency modulation. Riley and Laurence[3] also employed the narrow-gap approximation and investigated the stability boundary numerically using linear stability theory together with a Galerkin expansion and Floquet theory. Their results are in good agreement with the predictions of Hall. Moreover, they found certain parameter ranges where the

linear equilibrium solutions are harmonic and subharmonic, respectively. Carmi and Tustaniwskyj[4] and Tustaniwskyj and Carmi[5] used a similar approach as Riley *et al.* and also energy stability theory numerically. However, their results for a wide gap yielded a much larger negative threshold shift compared to previous investigations for a narrow gap. Such larger threshold shifts were also reported to be seen in experiments by Thompson[6] and more recently by Walsh *et al.*[7] The most recent experiments by Ahlers,[8] on the other hand, show threshold shifts that agree better with the smaller ones predicted by Hall.[2]

In contrast to the stability boundary of CCF nonlinear TVF had received much less attention in the past. On the theoretical side, Hall[2] derived an amplitude equation for the time dependence of slightly supercritical TVF while detailed experimental results on modulated TVF have been produced only very recently by Ahlers.[8]

Parallel to modulated Taylor-Couette flow there had also been much effort to explore the transition from a temperature-modulated heat-conductive basic state to time-dependent convection rolls in the Rayleigh-Bénard problem (see, for instance, Ahlers *et al.*[10,11] and the references cited therein). Although there are many analogies to TVF, there are also differences. For example, the modulation-induced shift of the threshold for onset of convention can be either positive or negative depending on the amplitude and frequency of the modulation. In particular, modulation of the temperature difference across the fluid layer with moderate amplitudes results in a relatively strong positive shift of the critical control parameter in contrast to the Taylor-Couette system. The stability characteristics and also the dynamics of nonlinear, time-dependent convection rolls have been quantitatively explained very well by a Lorenz-model ap-

proximation[10-12] of the Boussinesq equations. In view of this successful approach for Rayleigh-Bénard convection it seemed promising to describe also modulated TVF with similar model equations.

We therefore derive here a few-mode Galerkin-model approximation, which allows for a detailed understanding of the flow properties. Moreover, it is well suited to compare the results for TVF with those of Lorenz models for Rayleigh-Bénard convention. In addition and for comparison we simulate time-dependent TVF by integrating the full Navier-Stokes equations by a finite-difference method. Both methods permit large modulation amplitudes and strongly nonlinear TVF. Thus not only the stability boundary of CCF but also fully nonlinear TVF are investigated.

In Sec. II we describe the system and the two above-mentioned methods to investigate it. In Sec. III we briefly recall linear and nonlinear flow properties of the rotating Couette system under stationary driving obtained from our Galerkin model and the numerical simulation. Section IV contains our results for modulated driving. The stability threshold for onset of TVF as determined within the Galerkin approximation and from the numerical simulation is compared with experimental, numerical, and analytical results of other authors. For small modulation amplitudes and frequencies we elucidate similarities and differences of the stability properties of the modulated Bénard problem. Time-dependent and mean properties of fully nonlinear TVF above threshold are evaluated in the numerical simulation and in the model. The dynamics of the response to modulation is explained in great detail and compared with other available results and furthermore with the behavior of modulated convective flow in the Bénard system. Section V gives a summary of our results. In Appendix A we present details of the derivation of our Galerkin model and Appendix B discusses formal analogies of the TVF-model equations with the convective Lorenz-model equations.

II. METHODS OF INVESTIGATION

In this section we describe the system and our methods to investigate it.

A. System

We consider an incompressible fluid of density ρ and kinematic viscosity v between two concentric cylinders of radii R_1 and $R_2 > R_1$, gap width d, and radius ratio $\eta = R_1/R_2$. The flow is driven by rotating the inner cylinder with angular velocity

$$\Omega(t) = \Omega(1 + \Delta \cos\omega t) , \qquad (2.1)$$

which is allowed to vary harmonically in time around a mean value Ω with frequency ω and relative strength Δ. Throughout this work the outer cylinder is held at rest. We use

$$\epsilon = \frac{\Omega}{\Omega_c(\Delta = 0)} - 1 , \qquad (2.2)$$

the normalized deviation of the mean rotation rate Ω from the critical value for onset of TVF under stationary driving $\Omega_c(\Delta = 0)$ as a control parameter measuring the driving. To monitor the time dependence of the control parameter we also introduce

$$\epsilon(t) = \frac{\Omega(t)}{\Omega_c(\Delta = 0)} - 1 = \epsilon + (1 + \epsilon)\Delta \cos\omega t . \qquad (2.3)$$

Within our Galerkin approximation (Sec. II B) we describe a system of infinite axial extension whereas in our numerical simulation (Sec. II C) the system is finite with axial periodic boundary conditions. Our investigation is restricted to axisymmetric flow, because not only in the case of constant angular velocity but also for $\Delta \neq 0$ instability sets in axisymmetrically.[4,6-8] Furthermore, for stationary driving, $\Delta = 0$, the presence of axisymmetric vortices suppresses the onset of wavy, i.e., nonaxisymmetric vortex flow for a considerable range of control parameters especially for large radius ratios, although linear stability boundaries of CCF against axi- and nonaxisymmetric disturbances are rather close.[13] We assume the situation to be similar for periodic Taylor vortices and therefore we consider axisymmetric flow using cylindrical coordinates

$$\mathbf{u} = u(r,z,t)\mathbf{e}_r + [V(r,t) + v(r,z,t)]\mathbf{e}_\varphi + w(r,z,t)\mathbf{e}_z .$$
$$(2.4)$$

The basic CCF

$$V(r,t) = V_0(r) + \Delta V_1(r,t) , \qquad (2.5a)$$

$$V_0(r) = \frac{\eta}{1 - \eta^2} \left[\frac{r_2}{r} - \frac{r}{r_2} \right] , \qquad (2.5b)$$

$$V_1(r,t) = \frac{1}{2} \frac{J_1(\kappa r_2)Y_1(\kappa r) - Y_1(\kappa r_2)J_1(\kappa r)}{J_1(\kappa r_2)Y_1(\kappa r_1) - Y_1(\kappa r_2)J_1(\kappa r_1)} e^{-i\omega t}$$

$$+ \text{c.c.} \qquad (2.5c)$$

is harmonic with boundary conditions

$$V(r_1,t) = 1 + \Delta \cos\omega t, \quad V(r_2,t) = 0 , \qquad (2.5d)$$

at the inner and outer cylinder $r_1 = \eta/(1-\eta)$ and $r_2 = 1/(1-\eta)$, respectively. Here all quantities have been made dimensionless using the scales of Table I. J_1 and Y_1 are first-order Bessel functions and $\kappa = \sqrt{i\omega}$.

B. Galerkin approximation

To derive our Galerkin model we use the stream function $\psi(r,z,t)$, so that $u = \partial_z \psi$ and $w = -(\partial_r + 1/r)\psi$. Then the Navier-Stokes equations for the deviations, (u,v,w), from CCF, $(0,V,0)$, read

$$(\partial_t - \mathcal{D}\mathcal{D}_* - \partial_z^2)(\mathcal{D}\mathcal{D}_* + \partial_z^2)\psi - 2R^2 \frac{V}{r}\partial_z v$$

$$= 2R^2 \frac{v}{r}\partial_z v + \left[\frac{2}{r}(\partial_z \psi) + (\mathcal{D}_* \psi)\partial_z - (\partial_z \psi)\mathcal{D}_* \right]$$

$$\times (\mathcal{D}\mathcal{D}_* + \partial_z^2)\psi , \qquad (2.6a)$$

TABLE I. Characteristic scales.

Variable	Scale
r,z	d
t	$\dfrac{d^2}{\nu}$
u,w	$\dfrac{\nu}{d}$
ψ	ν
v	ΩR_1
p	$\dfrac{\rho \nu R_1 \Omega}{d}$

$$(\partial_t - \mathcal{D}\mathcal{D}_* - \partial_z^2)v + (\mathcal{D}_* V)\partial_z\psi = [(\mathcal{D}_*\psi)\partial_z - (\partial_z\psi)\mathcal{D}_*]v \ , \tag{2.6b}$$

with boundary conditions $v = \psi = \mathcal{D}_*\psi = 0$ at $r_{1,2}$. Here $\mathcal{D} = \partial_r$ and $\mathcal{D}_* = \mathcal{D} + 1/r$. The Reynolds number is defined in terms of the mean angular velocity Ω

$$R = \frac{R_1 \Omega d}{\nu} = (1+\epsilon)R_c(\Delta=0) \tag{2.7}$$

and $R_c(\Delta=0)$ is the critical one for onset of TVF under stationary driving.

We have approximated the preceding equations (2.6) with a Galerkin technique. The details are presented in Appendix A. Here we give a summary. From Galerkin-type linear-stability analyses it is known[14−16] that a very good approximation of the critical modes for $\Delta=0$ consists of

$$\psi = \hat{\psi}_{11}(t)|\psi_1(r)\rangle|\sqrt{2}\cos(kz)\rangle$$

together with

$$v = \hat{v}_{11}(t)|v_1(r)\rangle|\sqrt{2}\sin(kz)\rangle$$

in a Dirac bra and ket notation. Here $|\psi_1(r)\rangle$ and $|v_1(r)\rangle$ are orthogonal eigenfunctions of $(\mathcal{D}\mathcal{D}_*)^2$ and $\mathcal{D}\mathcal{D}_*$, respectively, subject to the above described boundary conditions. The orthogonal eigenfunctions $|\psi_n(r)\rangle$ and $|v_n(r)\rangle$ are in general cylindrical Chandrasekhar functions.[14] For a description of finite-amplitude TVF nonlinear interactions between these modes are essential. Such interactions, however, are possible only via modes $\hat{v}_{nm}(t)|v_n(r)\rangle|\sqrt{2}\sin(mkz)\rangle$ with $m=0,2$. Since, for slightly supercritical driving modes with $m=2$ are linearly damped very strongly, only modes $\hat{v}_{n0}(t)|v_n(r)\rangle$ provide effective coupling to the neutral modes. Moreover, in the narrow-gap limit $\eta \to 1$ the modes $\hat{v}_{n0}(t)|v_n(r)\rangle$ with $n \neq 2$ relax to zero, as can be seen from Eqs. (2.6). Thus the truncation

$$\psi(r,z,t) = \hat{\psi}_{11}(r)|\psi_1(r)\rangle|\sqrt{2}\cos(kz)\rangle \ , \tag{2.8a}$$

$$v(r,z,t) = \hat{v}_{11}(t)|v_1(r)\rangle|\sqrt{2}\sin(kz)\rangle$$

$$+ \hat{v}_{10}(t)|v_1(r)\rangle + \hat{v}_{20}(t)|v_2(r)\rangle \ , \tag{2.8b}$$

establishes a good approximation of nonlinear TVF at least for $\eta \simeq 1$ and for stationary driving ($\Delta=0$).

To describe modulated TVF with (2.8) requires the modulation to be sufficiently slow. If the modulation period is too small compared to the characteristic time for diffusing momentum radially across the gap then the flow is affected mainly in a boundary layer close to the inner cylinder that would not be properly described by (2.8) and that is analogous to the thermal Stokes layer in modulated convection.[17] Furthermore, we found[18] in numerical simulations at larger ω traveling-wave-like oscillations of the flow across the gap instead of the standing-wave-like oscillations at low ω. A *strong* upper limit for the frequencies admissible in our *model* would demand the Stokes-layer thickness not to fall below the gap width leading to $\omega \lesssim 2$.

Similar to Chen and Hsieh,[16] we project (2.6a) onto $\langle\sqrt{2}\cos(kz)|\langle\psi_1(r)|$ and (2.6b) onto $\langle\sqrt{2}\sin(kz)|\langle v_1(r)|$, $\langle v_1(r)|$, and $\langle v_2(r)|$, respectively. The resulting system of first-order ordinary differential equations for the amplitudes $\hat{\psi}_{11}(t)$, $\hat{v}_{11}(t)$, $\hat{v}_{10}(t)$, and $\hat{v}_{20}(t)$ has the form

$$\frac{\tau}{\sigma}\dot{X} = -X + \frac{\hat{t}}{s}Y[p(t) + \rho_1 W + \rho_2 Z] \ , \tag{2.9a}$$

$$\tau\dot{Y} = -Y + X[q(t) + \rho_3 W - Z] \ , \tag{2.9b}$$

$$\tau\dot{Z} = -b_2 Z + XY \ , \tag{2.9c}$$

$$\tau\dot{W} = -b_1 W + XY \ . \tag{2.9d}$$

Here $X(t)$, $Y(t)$, $Z(t)$, and $W(t)$ are the scaled amplitudes $\hat{\psi}_{11}$, $\hat{v}_{11}$, $\hat{v}_{20}$, and $\hat{v}_{10}$. The ρ_i are constants that involve Chandrasekhar functions and depend only on the radius ratio η, while σ, τ, s, b_1, and b_2 depend also on the axial wave number k. The coefficients $q(t)$ and $p(t)$ are harmonic in time: $q,p = 1 + \Delta A_{q,p}\cos(\omega t - \varphi_{q,p})$. For $\omega \to 0$ $A_{q,p} = 1$ and $\varphi_{q,p} = 0$. In the frequency range considered here the phases $\varphi_{q,p}$ are very small and vary slightly with modulation frequency ω and radius ratio η and $A_{q,p} \simeq 1$. Explicit formulas for all coefficients are given in Appendix A. Furthermore,

$$\hat{t} = T/T_c(\Delta=0) = (1+\epsilon)^2 \tag{2.9e}$$

is the Taylor number

$$T = \left[\frac{R_1 \Omega d}{\nu}\right]^2 \frac{d}{R_1} = R^2 \frac{1-\eta}{\eta} \tag{2.9f}$$

reduced by the critical one, $T_c(\Delta=0)$, for onset of TVF under stationary driving. Finally,

$$s(k) = T_{SB}(k, \ \Delta=0)/T_c(\Delta=0) \tag{2.9g}$$

is the reduced k-dependent stability boundary of CCF for stationary driving, $\Delta=0$, and given radius ratio η within the Galerkin approximation. The nonlinear model equations (2.9) were integrated in the case of modulated driving with a fourth-order Runge-Kutta scheme using up to 4000 steps per period.

C. Numerical simulation

In our numerical simulation of modulated axisymmetric flow we integrated a conservative version[19] of the

original Navier-Stokes equations that ensures correct momentum balance after discretization.[20]

We used the MAC method[20] to discretize velocity and pressure fields on three staggered grids in the r-z plane with uniform spacing $\Delta r = \Delta z = 0.05d$ between like points. Spatial derivatives are replaced by central differences and time derivatives by forward differences with a time step $\Delta t = \frac{1}{1800}$. To determine the pressure we use a variant[21] of the SOLA code.[22] Therein the explicitly advanced velocity and pressure are iteratively adjusted to each other using the continuity equation. This is equivalent to applying the artificial-compressibility method.[23]

Rigid boundary conditions were imposed at r_1 and r_2. In axial direction we used periodic boundary conditions with a periodicity length given by the critical wavelength $\lambda_c(\Delta=0, \eta=0.65)=2$ for onset of TVF under stationary driving. We fixed the arbitrary axial phase of the vortex pattern by requiring $w=0$ at $z=0$. Thus, in our numerical simulation as well as in our Galerkin model, we do not admit motion of the TVF pattern as a whole or "breathing" in such a way that the wavelength varies in time.

With our choice of the phase the radial flow has an extremum, e.g., a positive (negative) one at $z=0$ ($z=\lambda/2$). We checked for a few modulation parameters that the plane $z=\lambda/2$ remains a mirror plane as for stationary TVF such that the vortex above the plane is the mirror image of the one below it. In most simulations we therefore used this symmetry property and simulated only one vortex in the axial region $0 \leq z \leq \lambda/2$ with $z=\lambda/2$ being a mirror plane. In that way we of course suppress any flow that might break the symmetry between left and right turning vortices.

III. STATIONARY DRIVING

In this section we discuss the case of a constant rotation rate of the inner cylinder, $\Delta=0$. Then $p(t)=q(t)=1$ in our model.

A. Linear properties

As mentioned in Sec. II B our mode truncation yields quite accurate results for the linear-stability boundary of CCF. The neutral stability boundary within our model is $\hat{t}=s(k)$ or $T=T_{SB}(k, \Delta=0)$ (A4i). Calculations of the critical values k_c and $T_c=T_{SB}(k_c)=\min_k\{T_{SB}(k)\}$ for the range $\eta \in [\frac{1}{2}, 1]$ yield results (Fig. 1) that differ less than 1% and 3%, respectively, from high-precision numerical analyses.[13,24]

Our numerical simulations were done for $\eta=0.65$ where the critical wave number is close to $k_c=\pi$.[25] Extrapolation of growth rate γ of disturbances ($\sim e^{\gamma t}$) obtained within our numerical simulation yield a threshold $T_{SB}(\eta=0.65, k=\pi)=2985.4$ that is 1% smaller than the theoretical prediction by Roberts.[25] The deviation in our simulation is a consequence of the discretization of the Navier-Stokes equations. Throughout this paper the control parameters ϵ and $\hat{t}=(1+\epsilon)^2$ of the model and of the
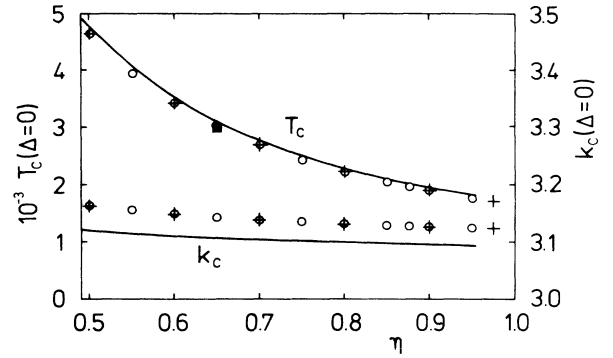

FIG. 1. Critical Taylor number and critical wave number for stationary driving, $\Delta=0$, vs radius ratio η. Solid lines denote the results of our Galerkin model. Open circles and crosses are the results of Refs. 13 and 24, respectively. The closed square denotes the critical Taylor number of our numerical simulation.

simulation are reduced by the appropriate respective critical values, $T_c(\Delta=0)$.

B. Taylor vortices

The amplitude of stationary TVF is given by the nontrivial fixed point of the model (2.9). As an example we consider TVF with the critical wave number $k=k_c$ so that $s=1$. Then

$$X = \pm \left\{ -\frac{1}{2b}\left[\hat{t}\left(1-\frac{a}{b}\right)-2 \right] \right.$$
$$\left. + \left\{ \frac{1}{4b^2}\left[\hat{t}\left(1-\frac{a}{b}\right)-2 \right]^2 + \frac{1}{b^2}(\hat{t}-1) \right\}^{1/2} \right\}^{1/2} ,$$

$$(3.1a)$$

$$Y = X/(1-bX^2), \quad Z = XY/b_2, \quad W = XY/b_1 , \quad (3.1b)$$

with $a = \rho_1/b_1 + \rho_2/b_2$ and $b = \rho_3/b_1 - 1/b_2$. For slightly supercritical driving, $\hat{t}-1 \ll 1$, Eqs. (3.1) may be expanded to yield, e.g.,

$$X = Y = \pm \left[\frac{\hat{t}-1}{-(a+b)} \right]^{1/2} + O(\hat{t}-1)^{3/2} . \quad (3.2)$$

Thus the velocity field amplitudes of slightly supercritical TVF vary in our model $\sim \sqrt{\epsilon}$ with $\epsilon = R/R_c - 1$. This behavior originally predicted by Davey[26] has been confirmed experimentally[27] and also in numerical simulations.[28]

To test our numerical simulation we made an axial Fourier analysis of u in the middle of the gap and of w at a quarter gap size away from the cylinder. We verified that the first two to three amplitudes $|U_n|$ and $|W_n|$ in the expansion

$$u(z) = \text{Re}\left[\sum_{n=1}^{\infty} U_n e^{ik_c nz} \right] ,$$

$$w(z) = \text{Re}\left[\sum_{n=1}^{\infty} W_n e^{ik_c nz} \right] ,$$

$$(3.3)$$

TABLE II. Small-ϵ behavior of axial Fourier amplitudes of TVF fields (3.3) in units of v/d under stationary driving for $\eta=0.65$ (cf. text for more details).

	$|U_1|/\sqrt{\epsilon}$	$|W_1|/\sqrt{\epsilon}$	$|U_2|/\epsilon$	$|W_2|/\epsilon$
Numerical simulation	15.15	17.67	11.2	6.22
Galerkin model	15.62	16.89		

increased $\sim\epsilon^{n/2}$ for small ϵ in accordance with the theory of Davey.[26] Table II shows that the Galerkin amplitudes of the first axial harmonic agree quite well with those of the numerical simulation. By construction [cf. Eq. (2.8)] our model does not contain higher axial harmonics.

In Fig. 2 we present for $\epsilon=0.306$ and $\eta=0.65$ a comparison of the *radial* variation of u, v, and w at the axial positions of their extrema. Note that the asymmetry of u and w is stronger in the numerical simulation than in the Galerkin model. This is related to the fact that the former properly reproduces the asymmetry between more intensive radial outflow and less intensive radial inflow while the model is restricted to just the basic axial harmonic, i.e., to symmetric radial inflow and outflow
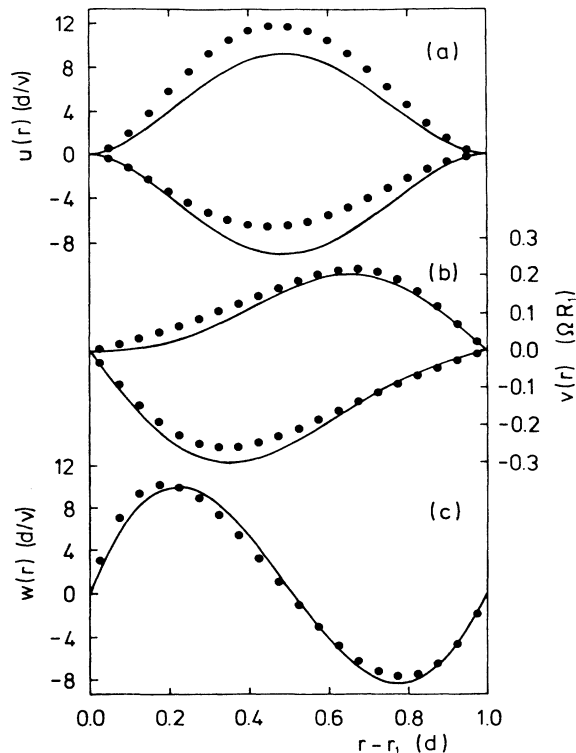

FIG. 2. Radial dependence of velocity profiles of unmodulated TVF ($\Delta=0$) obtained from the model Eqs. (2.9) (solid lines) and from the numerical simulation (closed circles) for $\eta=0.65$ and $\epsilon=0.306$. Plots have been made for axial positions, where (a) u, (b) v, and (c) w have an axial extremum. Note that v is the deviation of the azimuthal velocity from CCF. Quantities in parentheses are units.

profiles. With decreasing ϵ the asymmetry decreases and the agreement improves.

IV. TIME-DEPENDENT DRIVING

In this section we investigate the effects caused by modulation of the inner cylinder's angular velocity.

A. Stability of modulated CCF

We first investigate the shift of the stability boundary of CCF due to harmonic modulation $\Omega(t)=\Omega(1+\Delta\cos\omega t)$. A number of contributions have been devoted to the problem of the stability of modulated Couette flow.[1-9,29-32] Initiated by the experimental work of Donnelly,[1] who found the stability of Couette flow enhanced when the inner cylinder's angular velocity was modulated harmonically, most subsequent theoretical and experimental investigations indicate a destabilization of the basic flow. However, the reported threshold shifts differ significantly, as we shall discuss in detail after having presented our results.

1. Floquet theory for the model

The starting point for our model investigation is the linearized version of Eqs. (2.9). Since W and Z are damped exponentially, we have

$$\tau\dot{\mathbf{X}}=\begin{bmatrix} -\sigma & \sigma p(t)\dfrac{\hat{t}}{s} \\ q(t) & -1 \end{bmatrix}\mathbf{X} , \qquad (4.1a)$$

with $\mathbf{X}=(X(t),Y(t))$ or, equivalently,

$$\frac{\tau^2}{\sigma}\ddot{X}+\frac{\tau}{\sigma}\left[1+\sigma-\tau\frac{\dot{p}(t)}{p(t)}\right]\dot{X}$$

$$+\left[1-\tau\frac{\dot{p}(t)}{p(t)}-p(t)q(t)\frac{\hat{t}}{s}\right]X=0 . \qquad (4.1b)$$

The linearized Lorenz model for modulated convection[10] is identical to Eq. (4.1) with $\eta\to1$ except for the additional time dependence by the factor $p(t)$. The latter gives rise to different stability properties (cf. further below) and different nonlinear dynamics (see Sec. IV B).

The Floquet solution of (4.1a) has the form

$$\mathbf{X}(t)=\sum_{i=1}^{2} c_i e^{\mu_i t}\mathbf{P}_i(t) , \qquad (4.2)$$

where $\mathbf{P}_i$ are periodic functions with period $2\pi/\omega$. Floquet exponents μ_i have been determined by numerical integration of Eq. (4.1a) over one period from two orthogonal initial values $\mathbf{X}_1(0)=(1,0)$ and $\mathbf{X}_2(0)=(0,1)$. The stability boundary is identified by the vanishing maximum real part of the two eigenvalues. From this and additional analytical analyses we found that the modulation-induced shift, $T_{SB}(k,\eta,\Delta,\omega)-T_{SB}(k,\eta,\Delta=0)$, of the stability boundary of CCF depends only weakly on k and η. The main dependence comes from Δ and ω.

2. Determining $\hat{t}_c$ in the numerical simulation

In our numerical determination of the reduced critical Taylor number $\hat{t}_c(\Delta,\omega)=T_c(\Delta,\omega)/T_c(\Delta=0)$ we adopt a similar method as in the unmodulated case. For T close to T_c we assume basically an exponential growth or decay of small disturbances superimposed by oscillations due to the modulated driving. To calculate the overall growth rate, we averaged the radial velocity over one period of the modulation at a position (r_0,z_0) where it takes its maximum value. This procedure removed most of the oscillations. Next the averaged radial velocity was approximated by

$$A_0\exp\left[\gamma t + \sum_{n=1}^{3} c_n e^{-in\omega t}+\text{c.c.}\right]$$

using a least-square fit and $\hat{t}_c$ was then determined by extrapolating γ as a function of ϵ to zero.

This method is restricted to moderate modulation amplitudes because for large Δ a fit with only three Fourier modes in the preceding expression does not suffice. Also the modulation period should not be too large. If ω becomes comparable with γ the growth or decay of disturbances saturates already within about 1 period and γ cannot be determined by our averaging over a period. This method of evaluating the effective growth rate gives rise to precisely the same numerical problems and limitations when applied to the amplitude equation (cf. further below) which shows very similar dynamics while its threshold, $\hat{t}_c(\Delta)=1$, is known exactly. This enabled us to estimate the errors involved in determining $\hat{t}_c$.

3. Limit of small modulation amplitudes

Small modulation amplitudes can be treated within our model analytically. Calculations for arbitrary ω can be found in Ref. 30. An expansion in terms of Δ yields

$$\hat{t}_c(\Delta,\omega)=1+\Delta^2\hat{t}_c^{(2)}(\omega,k_c(\Delta=0))+O(\Delta^4) , \qquad (4.3a)$$

$$k_c(\Delta,\omega)=k_c(\Delta=0)+O(\Delta^2) . \qquad (4.3b)$$

In Fig. 3 we have plotted our results for $\hat{t}_c^{(2)}$ as function of ω. The curve obtained from our model $(\eta=1)$ is in good agreement with results of Hall[2] and of Riley and Laurence[3] if ω is less than, say, 5. Although the numerical results were obtained for $\eta=0.65$, the comparison seems to be justified, since all coefficients in Eq. (4.1) are only slightly dependent on η. The stabilization, $\hat{t}_c^{(2)}>0$, obtained in our model for $\omega\gtrsim7$ is due to the mode truncation: it does not resolve the Stokes layer structures at larger frequencies. Kuhlmann[30] has shown in calculations with idealized boundary conditions[31] that including higher radial modes leads to destabilization also at larger frequencies. We therefore, and in view of the discussion in Sec. II B, think that the present mode truncation restricts the *model's* application to low-frequency modulation.

Concerning our numerical simulation it should be noted that the growth rate analysis is not particularly well suited for a very precise stability analysis of modulated
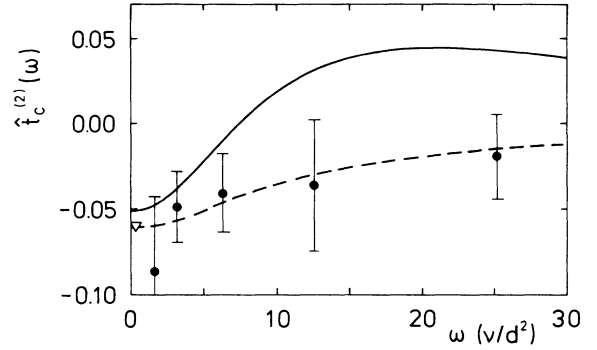
FIG. 3. Relative threshold shift $\hat{t}_c^{(2)}(\omega)$ [cf. Eq. (4.3a)] vs modulation frequency (in units of v/d^2). Solid curve results from a small-Δ expansion[30] of our model $(\eta=1)$. Closed circles show the quantity $[T_c(\Delta,\omega)/T_c(\Delta=0)-1]/\Delta^2$ obtained in our numerical simulation $(\eta=0.65)$ for small Δ. The dashed line and the open triangle are results for $\eta=1$ obtained by Hall (Ref. 2) and Riley and Laurence (Ref. 3), respectively.

CCF. This together with the rather small modulation-induced shift, $\Delta^2\hat{t}_c^{(2)}(\omega)$, of the threshold explains the large error bars. Nevertheless, we can conclude from our simulation that in the frequency range shown in Fig. 3 there is always destabilization of CCF by small-amplitude modulation.

4. Larger modulation amplitudes

In Fig. 4 we show the Δ dependence of $\hat{t}_c$ for larger Δ for our model (solid lines) as obtained with the Floquet method and for the numerical simulation (closed circles). The model's stability boundary is in the range $0.5\lesssim\eta\lesssim1$ independent of η within the line thickness and for $\omega<2$ it did not change anymore on the scale of Fig. 4(a). Note that $\hat{t}_c$ sharply drops off around $\Delta=1$. For smaller modulation amplitudes the destabilization is not so dramatic.

The critical wave number of our model shows only a weak Δ dependence: For small modulation amplitudes $k_c(\Delta)$ decreases quadratically in Δ and it reaches, e.g., for $\eta=1$ a minimum at $\Delta\simeq1.3$ with a minimum value 6.5% below $k_c(\Delta=0)$. The Δ variation for other η, however, is similar. Our curve for $k_c(\Delta, \omega=2, \eta=1)$ agrees very well with results of Riley and Laurence.[3] Since the neutral stability curve $\hat{t}_{SB}(k,\Delta)-\hat{t}_c(\Delta)$ is proportional to $[k-k_c(\Delta)]^2$ we shall ignore the effect of this shift $k_c(\Delta)-k_c(\Delta=0)$ of the critical wave number in the rest of this paper.

Within the investigated parameter range we have not found a primary subharmonic bifurcation out of the basic state, that is present in Rayleigh-Bénard convection.[10] However, we found in our model as well as in our numerical simulation for large Δ a secondary bifurcation from TVF with period $2\pi/\omega$ to TVF with period $4\pi/\omega$ when the direction of rotation of the inner cylinder is reversed during part of the period and $\epsilon(t)<-2$. For more details cf. Sec. IV B 9 below.
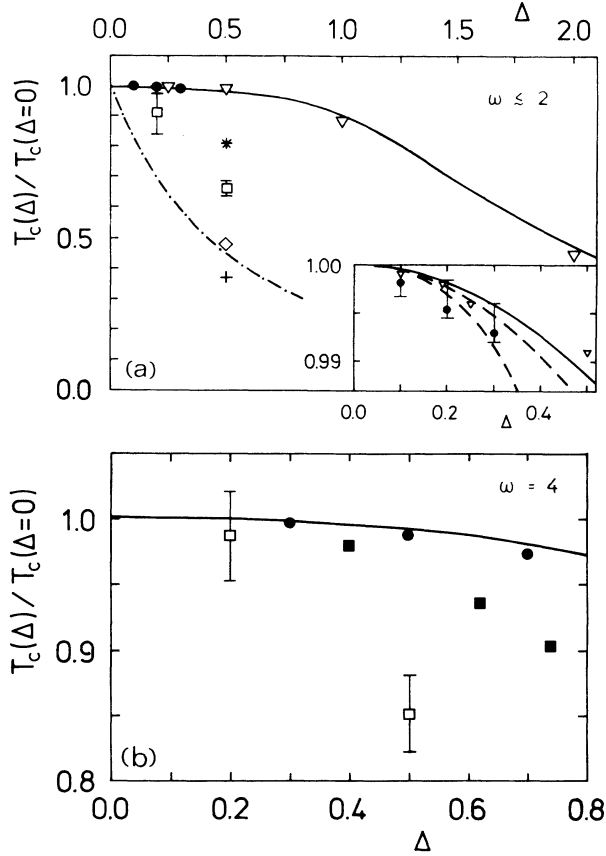
FIG. 4. Reduced critical Taylor number vs modulation strength Δ. Solid lines, our model ($\eta = 1$) for (a) $\omega = 2$ and (b) $\omega = 4$. Closed circles, our numerical simulation ($\eta = 0.65$) for (a) $\omega = \pi/2$ and (b) $\omega = 4$. Upper (lower) dashed curve in the inset, small-Δ expansion up to order Δ^2 (Δ^4) of Ref. 2 ($\eta = 1$, $\omega \rightarrow 0$). Open triangles, numerical stability analysis of Ref. 3 ($\eta = 1$, $\omega = 0.2$). Plus (star), numerically obtained strong (mean) energy limit of Ref. 5 ($\eta = 0.693$, $\omega = 2$). Diamond, linear stability boundary given in Ref. 4 ($\eta = 0.693$, $\omega = 2$). There also $\hat{t}_c(\Delta, \omega \rightarrow 0) = (1 + |\Delta|)^{-2}$ (dot-dashed line) was suggested. Open squares, experimental results ($\eta = 0.719$) for (a) $\omega = 2.21$ and (b) $\omega = 4$ of Ref. 7. Closed squares, experimental results ($\eta = 0.75$, $\omega = 4$) of Ref. 8. Note the different scales in (a) and (b).

5. Comparison with other authors

In Fig. 4 we compare our results for $\hat{t}_c(\Delta, \omega)$ with experiments and other theoretical results. Since $\hat{t}_c$ is practically independent of η the comparison of data obtained for different η is justified. On the theoretical side there is very good agreement between model, numerical simulation, the linear stability analysis of Riley and Laurence,[3] and the small-Δ expansion of $\hat{t}_c$ by Hall[2] for $\omega \rightarrow 0$. These approaches show that the stability threshold $\hat{t}_c(\Delta, \omega)$ of CCF has already reached in the frequency range $\omega \simeq 2$ its $\omega \rightarrow 0$ asymptotic behavior.

This is in marked contrast to the asymptote $\hat{t}_c(\Delta, \omega \rightarrow 0) = (1 + |\Delta|)^{-2}$ (dot-dashed line) proposed by Thompson,[6] Carmi and Tustaniwskyj,[4] and Walsh et al.[7] Such a behavior of the threshold for onset of secondary

flow might be linked[11,33] to the presence of imperfections (of geometrical origin, sidewalls, convection, thermal noise, etc.): The flow disturbances of the pure CCF state resulting from symmetry-breaking imperfections provide finite amplitude perturbations from which TVF starts growing during the supercritical phase, $\Omega(t) > \Omega_c(\Delta = 0)$, of the driving. Since $\Omega(t) = \Omega(1 + \Delta \cos\omega t)$ is in the limit $\omega \rightarrow 0$ sufficiently long supercritical to develop TVF starting from finite disturbances as soon as $\Omega(1 + |\Delta|) > \Omega_c(\Delta = 0)$ one thus expects $\hat{t}_c = (1 + |\Delta|)^{-2}$ to be the threshold for appearance of TVF in the $\omega \rightarrow 0$ limit. Without imperfections, however, there is no lower limit for TVF amplitudes. In our simulation, for example, they decay to zero starting from finite initial values during the subcritical driving phases whenever T is below the threshold for the perfect system. If the above described picture is correct then symmetry-breaking experimental imperfections might account, at least partly, for the differences in Fig. 4 between (our) theoretical threshold for onset of TVF and the experiments by Walsh et al.[7] (open squares) and by Ahlers[8] (closed squares). With increasing ω these differences should, however, decrease, as will be discussed later on.

6. Comparison with the modulated Bénard problem

It is very instructive and elucidating to compare the stability properties of modulated CCF with those of the basic conductive state in the Rayleigh-Bénard system under temperature modulation. The comparison can be made most easily in the limit $\omega \rightarrow 0$.

For small frequencies the modulated CCF profile $V_1(r, t)$ oscillates in phase with the driving as does the analogous conductive temperature profile. Thus the phase difference between $p(t)$ [Eq. (A4f)] and $q(t)$ [Eq. (A4g)] vanishes and $p(t) = q(t) = 1 + \Delta \cos\omega t$. If, furthermore, Δ is small then Eq. (4.1b) reduces to the standard Mathieu equation

$$m\ddot{X} + m\Gamma\dot{X} - (\alpha + \Delta\beta\cos\omega t)X = 0 , \quad (4.4a)$$

with

$$m = \frac{\tau^2}{\sigma}, \quad \Gamma = \frac{1+\sigma}{\tau}, \quad \alpha = \left[1 + \frac{\Delta^2}{2}\right]\hat{t} - 1, \quad \beta = 2\hat{t} . \quad (4.4b)$$

Here we have used $s = 1$ for $k = k_c(\Delta = 0)$. In deriving (4.4) from (4.1b) we have ignored $\dot{p}$ and a term $\sim \Delta^2\cos 2\omega t$ in comparison with $\Delta\cos\omega t$.

Such an equation was shown[10] to yield the stability threshold of the conductive state, $X = 0$, in the Bénard system to a very high accuracy. For $\omega \rightarrow 0$ and small Δ the stability boundary of the $X = 0$ basic solution is given in the $\alpha - \beta$ plane by

$$\alpha_c(\Delta, \omega \rightarrow 0) = \Delta^2 \frac{\beta^2}{2m\Gamma^2} + O(\Delta^4) . \quad (4.5)$$

The modulation-induced stabilization,

$$\alpha_c(\Delta, \omega \rightarrow 0) > \alpha_c(\Delta = 0) ,$$

is an inertia effect[10,34] caused by the presence of the

second-derivative term in (4.4a). In the Rayleigh-Bénard system $\beta = \hat{r}$ and $\alpha = \hat{r} - 1$ are given by the mean reduced Rayleigh number $\hat{r} = \overline{\mathcal{R}(t)}/\mathcal{R}_c(\Delta = 0)$. Then the stabilization of the basic conductive state by the above-mentioned inertia effect is fully operative: $\hat{r}_c(\Delta) = 1 + \Delta^2/(2m\,\Gamma^2) + O(\Delta^4)$. In the modulated Couette problem, however,

$$\alpha = \left[1 + \frac{\Delta^2}{2}\right]\hat{t} - 1 = \frac{\overline{T(t)}}{T_c(\Delta = 0)} - 1 = \frac{\overline{\Omega^2(t)}}{\Omega_c^2(\Delta = 0)} - 1$$

(4.6)

is determined by the mean Taylor number, i.e., by the mean of the squared rotation rate rather than by the mean rotation rate $\overline{\Omega(t)}$ itself. Thus the effective control parameter governing the stability of CCF at least for $\omega \to 0$ and small Δ is shifted upwards by the amount $(\Delta^2/2)\hat{t}$ relative to $\hat{t}$. The trivial modulation enhancement of the mean Taylor number via $\overline{\Omega^2(t)} = \overline{\Omega(t)}^2(1 + \Delta^2/2)$ is larger than the inherent inertia-induced stabilization, albeit only by a very small amount. The former has a relative size $\Delta^2/2$ whereas the latter is $\Delta^2\beta^2/(2m\,\Gamma^2) = \Delta^2 2\sigma/(\sigma + 1)^2 = 0.45\Delta^2$ if one expands $\hat{t}_c$ up to second order in Δ. The net effect is a very small destabilization

$$\hat{t}_c(\Delta, \omega \to 0) = 1 - \frac{\Delta^2}{2}\left[\frac{\sigma - 1}{\sigma + 1}\right]^2 + O(\Delta^4) \ . \qquad (4.7)$$

The corresponding value of $t_c^{(2)}(\omega \to 0) = -0.05$ agrees qualitatively with the linear stability analyses of Hall,[2] Kumar et al.,[32] and Bhattacharjee et al.[29]

B. Taylor vortex dynamics

Here we discuss the time-periodic nonlinear TVF in the presence of modulation. We have investigated only such parameters that the system reaches the limit cycle within a few radial diffusion times. We mostly restrict ourselves to a radius ratio $\eta = 0.65$ and a fixed wave number $k = k_c(\Delta = 0)$.

1. Reduced quantities

In Sec. IV B we shall consider reduced quantities, e.g., the quotient $w(r,z,t,\Delta)/w(r,z,\Delta = 0)$ of the axial velocity at a particular point (r,z) divided by w at the same point for unmodulated driving or the quotient of axial Fourier modes, etc. We found that these reduced quantities depend only very weakly on η and we checked that differences with the case $\eta = 1$ are negligible for the investigated parameter range. We first investigate modulation with the low frequency $\omega = \pi/2$ that is sufficiently small for our model to be valid. Since properties are not expected to vary much in the vicinity of $\omega = \pi/2$ our results for $\eta = 0.65$, $k = k_c(\Delta = 0)$, and $\omega = \pi/2$ should be typical for a wide range of other parameter combinations.

For a comparison of results from our Galerkin model and the numerical simulation we have chosen the axial velocity at a position (r_0, z_0) where $w(r,z,\Delta = 0)$ is maximal. In the driving range considered in this work we found in our numerical simulation $r_0 \simeq 0.25$ and z_0 to be the axial position of a vortex center. We consider the re-

duced axial velocity

$$\hat{w}(t) = \frac{w(t)}{w(\Delta = 0)}\Big|_{r_0, z_0} \qquad (4.8)$$

to be an appropriate time-dependent order parameter for monitoring the response of the flow to modulation of the driving. In our model $\hat{w}(t)$ is given by

$$\hat{w}(t) = \frac{X(t)}{X(\Delta = 0)} \ . \qquad (4.9)$$

The quotient $w(r,z,t)/w(r,z,\Delta = 0)$ is independent of r and z in the model and almost independent in the numerical simulation. Therefore the fact that the Galerkin model yields a slightly different location of maximal axial flow due to the mode truncation [cf. Fig. 2(c)] is irrelevant. We furthermore checked that the time dependence of the first axial harmonic $w_1(r,t)$ when reduced by $w_1(r, \Delta = 0)$ agrees within pencil's width with $\hat{w}(t)$ [Eq. (4.8)].

The time dependence of the reduced radial velocities $u(t)/u(\Delta = 0)$ at particular points and of its reduced Fourier modes is almost identical with that of $\hat{w}(t)$. Thus the spatial structure of the Taylor vortex in the r-z plane is unchanged by the modulation. It is only the flow amplitude that periodically varies. The absence of modulation-induced structural changes might be partly enforced by the fact that in our model, as well as in our numerical simulation, the axial wavelength of the TVF is fixed. In fact, modulation-induced deformations of the Taylor vortices are not completely absent in our numerical simulation. If within a modulation cycle the largest rotation rate of the inner cylinder significantly exceeds the critical one, $\Omega_c(\Delta = 0)$, then higher axial harmonics have a time dependence that differs slightly from the basic axial Fourier mode.

For comparison we also integrated an amplitude equation

$$\tau_0 \partial_t A = [\epsilon(t) - gA^2]A \ , \qquad (4.10)$$

with the time-dependent control parameter (2.3), which is related to $\hat{r}$ by

$$\epsilon(t) = \frac{\Omega(t)}{\Omega_c(\Delta = 0)} - 1 = (\hat{r})^{1/2}(1 + \Delta \cos\omega t) - 1 \ . \qquad (4.11)$$

The inverse time scale is $\tau_0^{-1} = 26.45$ according to Dominguez-Lerma.[35] To rewrite (4.10) into an equation for the reduced axial velocity $\hat{w}(t) = A(t)/A(\Delta = 0)$ one can identify $g = \epsilon/A^2(\Delta = 0)$.

2. Time dependence of $\hat{w}(t)$

In Fig. 5 we show $\hat{w}(t)$ over one period. In the upper part we have plotted $\epsilon(t)$ as a reference. Note that for $\epsilon(t) > 0$ the driving is larger than the static critical one, $\Omega_c(\Delta = 0)$. We shall describe this situation by saying that the driving is supercritical.

The shape of $\hat{w}(t)$ depends on the fraction of time for which $\epsilon(t) > 0$ compared to the time, when $\epsilon(t) < 0$, and on the maximum and minimum values of $\epsilon(t)$. For large mean rotation rates and small modulation amplitudes, i.e., for ϵ larger than Δ, the driving is supercritical all the time and $\hat{w}(t)$ oscillates around a mean value with small
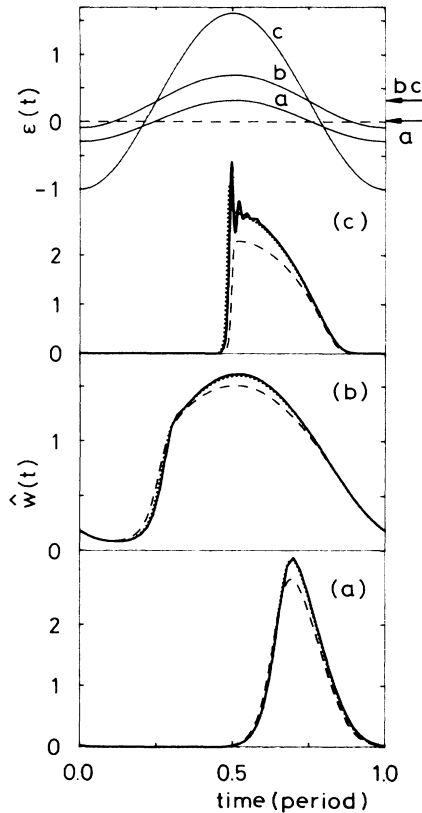
FIG. 5. Normalized axial velocity $\hat{w}$ as function of time for (a) $\epsilon=0.016$, $\Delta=0.3$; (b) $\epsilon=0.306$, $\Delta=0.3$; (c) $\epsilon=0.306$, $\Delta=1.0$. Solid line, model solution; dotted line, numerical simulation; dashed line, amplitude equation. The radius ratio is $\eta=0.65$ and modulation frequency is $\omega=\pi/2$. The upper part shows the respective control parameter $\epsilon(t)=\Omega(t)/\Omega_c(\Delta=0)-1$. Arrows indicate the mean $\overline{\epsilon(t)}=\epsilon$.

amplitude. The response is more interesting when Δ becomes larger. In Fig. 5(a) we have plotted $\hat{w}(t)$ for $\Delta=0.3$ and $\epsilon=0.016$ so that times during which the driving is supercritical and subcritical are nearly the same. We notice a maximum of $\hat{w}(t)$ at times immediately before $\epsilon(t)$ changes sign from positive to negative, and the rising slope of $\hat{w}(t)$ is a little bit steeper than the falling one. It takes nearly half the period for $\hat{w}$ to grow to significant order once having reached very low values during the damping phase $\epsilon(t)<0$. For $\Delta=0.3$ and $\epsilon=0.306$ [Fig. 5(b)] the driving is almost always supercritical. Most of the time the TVF intensity $\hat{w}(t)$ follows adiabatically the instantaneous supercritical driving $\epsilon(t)$ and the maxima of both curves coincide. However, the rising slope of $\hat{w}(t)$ has become considerably steeper than the falling one and a small bump appears in the former. This effect is much more pronounced for $\Delta=1$ and $\epsilon=0.306$ [Fig. 5(c)]. There we have a strong subcritical damping phase during which $\hat{w}(t)$ nearly drops to zero. Then it takes about half the time in which $\epsilon(t)$ is positive for the flow to grow again from the previous small amplitudes to appreciable size. In the growth phase $\hat{w}(t)$ increases very sharply just before $\epsilon(t)$ reaches its maximum. This sharp jumplike increase of the amplitude seems to

cause an overshoot with a few subsequent relaxational oscillations. Then, during the downswing of the driving, the amplitude $\hat{w}(t)$ adiabatically follows the driving almost until $\epsilon(t)$ becomes negative. A similar sharp increase of the flow intensity followed by oscillations has also been observed by Neitzel[36] during sudden-start numerical computations of TVF and by Cooper et al.[37] during experiments in which $\Omega(t)$ was ramped linear in t.

Figure 5 shows the excellent agreement between model and the numerical simulation of the full equations. We presume that the differences in the amplitude of the overshoot result from damping by coupling to modes that are present in the numerical simulation but discarded in our Galerkin model.

When this paper was written up Ahlers communicated recent results[8] of his modulated TVF experiments for $\eta=0.75$. He measured the axial velocity field as a function of z at a radial position about a quarter gap size inwards from the inner cylinder and then determined the first axial Fourier component $W_1(t)$. In Fig. 6 we compare for the common frequency $\omega=4$ his results (circles) with our simulation (solid line) for two common representative combinations of the driving parameters. However, in our case $\eta=0.65$. To make the comparison we determined $W_1(t)$ and then normalized it by $W_{10}(\Delta=0)$ which is the leading coefficient in the expansion of

$$W_1(\Delta=0)=\sqrt{\epsilon}\,W_{10}(\Delta=0)+O(\epsilon) \qquad (4.12)$$

in powers of $\sqrt{\epsilon}$. It is gratifying to see that the simulation of just one Taylor vortex as described in Sec. II C yields quantitatively the same results as the experiment.
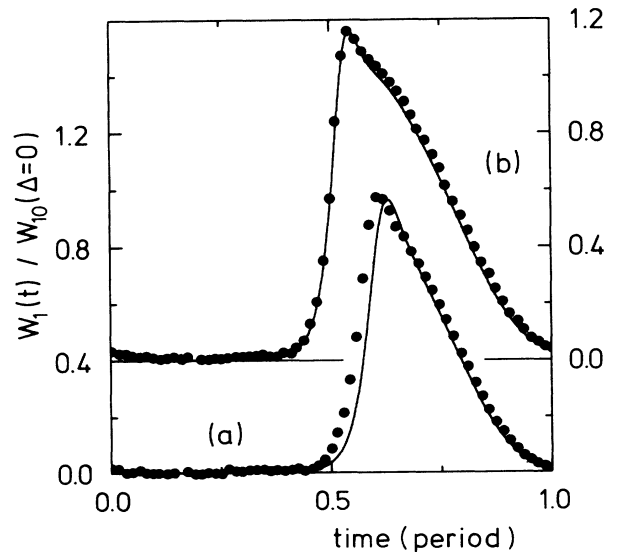

FIG. 6. Comparison of the reduced axial Fourier component $W_1(t)$ resulting from our numerical simulation ($\eta=0.65$, lines) and from experiments ($\eta=0.75$, dots) of Ahlers (Ref. 8) both done with the same $\omega=4$, $\delta=(1+\epsilon)\Delta=0.7$, and (a) $\epsilon=0.1$ and (b) $\epsilon=0.2$. The quantity $W_{10}(\Delta=0)$ is defined in Eq. (4.12). The time origin is fixed as in Fig. 5 by a minimum in $\epsilon(t)$.

3. Dynamics of the response to modulation

To elucidate the dynamics of the response $\hat{w}(t)$ to modulation let us consider the model equations given the fact that their results almost coincide with those of the numerical simulation. There are two explicit time scales involved in the model equations (2.9). One is the fast intrinsic time scale $\tau \simeq 0.05$ (cf. Table III) of TVF. The other characteristic time is a long one in comparison with τ, namely, the period of modulation $2\pi/\omega > 1$ for all modulation frequencies considered here.

Let us therefore first discuss the limit in which the TVF amplitude $\hat{w}(t)$ follows adiabatically the driving. This assumption is of course valid only as long as the driving $\epsilon(t)$ is always sufficiently supercritical, since $\hat{w}(t)$ decays basically exponentially towards zero whenever $\epsilon(t)$ is subcritical. In the adiabatic approximation the instantaneous mode amplitudes $X^*(t)$, $Y^*(t)$, $Z^*(t)$, and $W^*(t)$ follow from the model equations (2.9) by ignoring the time derivatives, e.g.,

$$(X^*)^2 = -\frac{1}{2b}\left[\hat{\tau}\left[pq - \frac{a}{b}q^2\right] - 2\right]$$
$$+ \left\{\frac{1}{4b^2}\left[\hat{\tau}\left[pq - \frac{a}{b}q^2\right] - 2\right]^2\right.$$
$$\left. + \frac{1}{b^2}(\hat{\tau}pq - 1)\right\}^{1/2} . \qquad (4.13)$$

The constants a and b are given below Eqs. (3.1). In Figs. 7(b) and 7(c) we show $X^*(t)/X(\Delta=0)$ in comparison with the full solution of Eqs. (2.9a)–(2.9d). Once the amplitude has grown sufficiently it is identical to the quasi-stationary fixed point given by Eqs. (4.13) apart from initial oscillations. The adiabatic approximation falls if $\epsilon(t)$ is sufficiently long subcritical. The delay of the appearance of fully developed TVF relative to $\epsilon(t)$ is due to the fact that the amplitude $\hat{w}(t)$ becomes extremely small
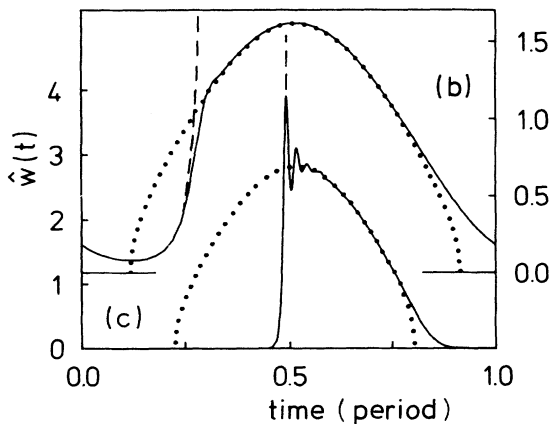

FIG. 7. Comparison of the normalized axial velocity $\hat{w}$ with the adiabatic approximation Eq. (4.13) (dots). Dashed lines show the dynamics of the linearized model equations with initial values taken from the full nonlinear model. Parameters for b and c are those of Figs. 5(b) and 5(c), respectively.

during the subcritical driving phase of the cycle, e.g., $\hat{w} < 10^{-12}$ for $\Delta = 1$ and $\epsilon = 0.306$. Furthermore, the time when $\hat{w}(t)$ reaches its minimum and starts growing is slightly delayed in our model from the time when $\epsilon(t)$ changes sign. The delay time being given by the first zero of $(X^*)^2 = 0$. As can be seen from Fig. 7 the adiabatic approximation is slightly out of phase with the driving $\epsilon(t)$. This shift is due to the phases φ_p and φ_q and vanishes for $\omega \rightarrow 0$.

For those parameters where $\hat{w}(t)$ has enough time to drop to infinitesimally small values the subsequent growth behavior in the supercritical phase of each modulation cycle is determined by linear equations. To show this we integrated the linearized model equations (4.1) starting at the time where $X^*(t) = 0$ with initial values taken from the nonlinear limit cycle. The resulting dashed curves in Fig. 7 show the same growth behavior up to the overshoot as the full equations.

4. Overshoot and oscillations of $\hat{w}(t)$

A qualitative understanding of the oscillations in $\hat{w}(t)$ following the overshoot may be gained from a simplification of our model equations (2.9). For small frequencies Z can be integrated out.[10,38] W vanishes for $\eta \rightarrow 1$ (cf. Appendix B) and it is still small in the investigated η range. Neglecting a memory term in that integration which is reasonable if variations of X are small on a time scale τ/b_2, we arrive at an anharmonic oscillator equation

$$m\ddot{X} + m\Gamma\dot{X} - [\hat{\tau}p(t)q(t) - 1]X + \frac{1}{b_2}X^3 = 0 , \qquad (4.14)$$

with $m = \tau^2/\sigma \simeq 1.34 \times 10^{-3}$, $\Gamma = (1+\sigma)/\tau \simeq 57.7$, and $b_2 \simeq 2$. It describes a "particle" of "mass" m moving in the presence of "friction" Γ in a time-dependent potential

$$[1 - p(t)q(t)\hat{\tau}]X^2/2 + X^4/(4b_2) .$$

Because of the parametric modulation the form of the potential periodically changes, e.g., from a configuration with a single central minimum to a double well with a central maximum. Small deviations from the instantaneous position of the potential minimum at

$$X^*(t) = \sqrt{b_2[\hat{\tau}p(t)q(t) - 1]} \qquad (4.15)$$

vary like $e^{\gamma^* t}$ with

$$\gamma^* = -\frac{\Gamma}{2} \pm \left[\frac{\Gamma^2}{4} + \frac{2}{m}[1 - \hat{\tau}p(t)q(t)]\right]^{1/2} . \qquad (4.16)$$

The expression for γ^* gives the local frequency and relaxation rate to the "fixed point" X^* [Eq. (4.15)]. For $\Delta = 0.3$ and $\epsilon = 0.016$ γ^* is real nearly all the period whereas for $\Delta = 0.3, 1.0$ and $\epsilon = 0.306$ (cf. Fig. 5) oscillations occur or at least a "nose" is forming.

5. Comparison with the amplitude equation

We now turn to the results of the amplitude equation (4.10). First of all we observe that the peak values of $\hat{w}(t)$ predicted by this equation are too small. This can partly

be traced back to the low-order expansion of nonlinearities, dealing merely with $\sqrt{\epsilon(t)}$ terms in quasistationary states. Especially for large values of $\hat{w}(t)$ higher-order terms cannot be ignored (see also Fig. 11 below), whereas the relative differences decrease when $\hat{w}(t)$ becomes smaller. Second, the TVF sets in later within the amplitude-equation approximation since the latter misses the destabilization of CCF by modulation that is present in the model and the numerical simulation. Therefore, the growth rates of $\hat{w}(t)$ calculated from the amplitude equation are smaller than those calculated from the model or from our numerics. But the fact that there is a sharp increase of $\hat{w}(t)$ is properly reproduced. Also the phase difference between the response $\hat{w}(t)$ and the driving $\epsilon(t)$ is reasonably well reproduced by the amplitude equation. In particular, for small ϵ and Δ the response varies $\sim e^{(\Delta/\omega)\sin\omega t}$, i.e., like in Fig. 5(a) as predicted[10] by the amplitude equation close to threshold. The lack of overshoot and subsequent oscillations results from the slowly varying amplitude approximation leading to a *first-order* differential equation that has no inertia effects. Thus Galerkin model calculations and numerical simulation clearly demonstrate that the amplitude equation (4.10) is inferior to the former.

6. Frequency dependence of the response $\hat{w}(t)$

So far we have discussed the response $\hat{w}(t)$ of the TVF to rather low-frequency modulation. In Fig. 8 we show how the shape of our numerically simulated $\hat{w}(t)$ changes
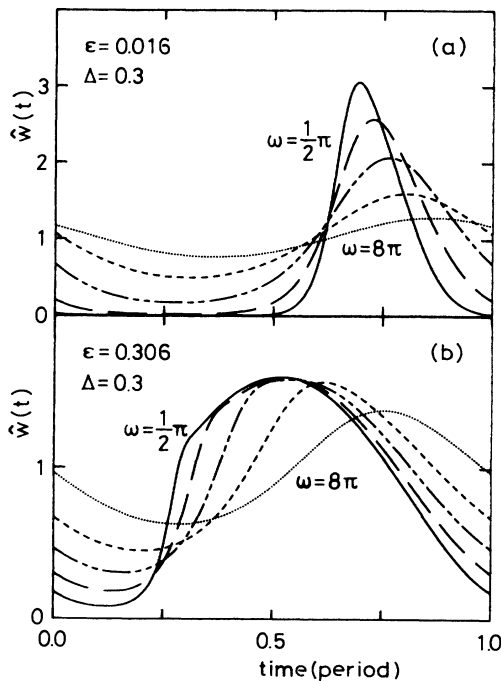

FIG. 8. Normalized axial velocity $\hat{w}(t)$ of the numerical simulation ($\eta=0.65$) vs time for frequencies $\omega=\pi/2$ (solid curve), π (long-dashed curve), 2π (dot-dashed curve), 4π (short-dashed curve), 8π (dots). The time origin is fixed by a minimum in $\epsilon(t)$.

with frequencies increasing from $\omega=\pi/2$ to 8π for two representative combinations of the driving parameters: (a) $\epsilon \ll \Delta$ and (b) $\epsilon \simeq \Delta$. In each case the response $\hat{w}(t)$ to the driving becomes more harmonic and the phase shift of the peak position of $\hat{w}$ relative to that of $\Omega(t)$ increases with increasing ω. We also found[18] that with increasing ω the TVF fields show more and more traveling-wave behavior across the gap. The deviations from CCF propagate radially leading to radial phase differences of the response while for small ω the TVF fields oscillate more in a standing-wave manner with globally varying amplitudes.

Since for (b) the driving is always supercritical there is a sizable TVF amplitude—$\hat{w}(t)$ in Fig. 8 is a reduced quantity—during all the period. Also, for small ω the response follows quasiadiabatically the moving fixed point after a short rapid growth as described in Sec. IV B 3. For ϵ near the threshold (a), however, the effective driving and with it the effective growth rates are smaller and the occurrence of sizable TVF lags behind the maximum of the driving. Furthermore, the minimum amplitudes during a cycle rapidly decrease with decreasing ω reaching sooner or later the imperfection-generated disturbance flow level in experiments.

7. Experimental observability

Neither in our model nor in our numerical simulation are there end-wall-induced Ekman vortices or geometrical imperfections or other forms of forces that break the axial translational invariance. This allows, in particular for small ω, the TVF amplitudes to become infinitesimally small during the subcritical part of each modulation cycle thus giving rise to the peculiar response dynamics of $\hat{w}(t)$ shown in Figs. 5–7. Hence, to observe this behavior experimentally it is absolutely necessary to suppress inhomogeneities that cause premature onset of TVF during modulation. For example, it might be necessary to eliminate the Ekman vortex system induced by rigid end plates, e.g., by employing conical ends[39] that let the effective driving taper off to subcritical values. We expect a periodic "breathing" of the Ekman vortex system, i.e., TVF intensity fronts[19,40,41] propagating inwards into the annulus during each supercritical phase of a modulation cycle. But even in the absence of end-wall-generated vortex fronts the remaining imperfections in an experimental setup might be sufficiently large to cause a response of $\hat{w}(t)$ that is—in particular for small ω—dominated by this forcing rather than by the intrinsic TVF dynamics. Also random forcing has been invoked to explain growth of flow patterns in the rotating Couette system[37] and the Bénard system.[42,43]

8. Comparison with the modulated Bénard problem

Although the response of convection rolls in the Rayleigh-Bénard problem represented by, e.g., Lorenz models to low-frequency modulation of the driving force is similar to that of Taylor vortices, there are differences. To elucidate these differences and the analogies we shall consider our Galerkin model in the narrow gap limit, $\eta\rightarrow 1$. Then the mathematical expressions defining our

model simplify and may be compared directly with analogous Lorenz models[10,44] for convection (cf. Appendix B). It is important to note that in doing so one does not lose physical substance since the reduced quantities, such as $\hat{w}$, practically do not differ from the corresponding ones for $\eta \neq 1$.

Further simplification arises for low-frequency modulations. One may verify by direct numerical comparison that then the Galerkin model equations are reasonably well approximated by the parametrically modulated anharmonic oscillator (4.14) with $p(t)$ and $q(t)$ replaced by the low-frequency limit $p(t) = q(t) = 1 + \Delta \cos \omega t$. Also the Lorenz model for modulated Rayleigh-Bénard convection[10,44] (RBC) reduces for small frequencies to such an equation (cf. discussion in Sec. II B of Ref. 10). In fact, the approximation of the model by a modulated anharmonic oscillator is better for convective rolls than for Taylor vortices.

To make the comparison we consider the reduced amplitude $\hat{w}(t) = X(t)/X(\Delta = 0)$ of the axial TVF velocity field or of the vertical convective velocity, respectively. The TVF amplitudes for stationary driving are given by $X^2(\Delta = 0) = b_2(\hat{t} - 1) \simeq 2[(1 + \epsilon)^2 - 1]$ according to (4.15). The convective flow amplitude in the absence of temperature modulation, on the other hand, is given by $X^2(\Delta = 0) = \mathcal{R}/\mathcal{R}_c(\Delta = 0) - 1 = \epsilon$. Here we imply a correspondence between Reynolds number R and Rayleigh number $\mathcal{R}$ in the two systems. With this notation the anharmonic-oscillator approximation is modulated TVF and RBC reads

$$m\ddot{\hat{w}} + m\Gamma\dot{\hat{w}} - [(1 + \epsilon)^n(1 + \Delta \cos \omega t)^n - 1]\hat{w}$$
$$= -[(1 + \epsilon)^n - 1]\hat{w}^3, \quad (4.17)$$

with $n = 1$ for RBC and $n = 2$ for TVF. For a fluid of unit Prandtl number the coefficients $m \simeq 1.36 \times 10^{-3}$ and $\Gamma \simeq 57.3$ are the same for both systems.

We should like to stress again that the approximation of the Galerkin equations by (4.17) is reasonable only for low-frequency modulation, not too large mean driving ϵ, and not too large modulation amplitudes Δ (and not too small radius ratios in the rotating Couette system). But the reduction to a common simple equation is a very useful means to discuss qualitatively the differences and similarities in the response of the vortex flows in these systems.

The most important difference comes from the different way in which the modulation of the driving couples to the amplitude $\hat{w}(t)$ of the vortex velocity field. In the Rayleigh-Bénard system the time-dependent Rayleigh number enters linearly via $\mathcal{R}(t)/\mathcal{R}_c(\Delta = 0) = (1 + \epsilon)(1 + \Delta \cos \omega t)$ into the parametric modulation of the "potential" that the amplitude "sees" in (4.17). In the rotating Couette system the rotation rate of the inner cylinder enters quadratically via the Taylor number $T_a(t)/T_{ac}(\Delta = 0) = (1 + \epsilon)^2(1 + \Delta \cos \omega t)^2$. Hence the TVF amplitude $\hat{w}(t)$ is subject to a forcing that is larger in size and, moreover, has a different time dependence than the forcing of convective vortices. As discussed already in Sec. IV A 6 it is this difference that causes the modulation-induced downward shift of the threshold

$\epsilon_c(\Delta, \omega)$ for onset of TVF as compared to the upwards threshold shift for onset of RBC. Moreover, in the driving range $\epsilon > \epsilon_c(\Delta, \omega)$ where vortex flow is present in both systems the difference in driving leads to larger TVF amplitudes. For example, for the parameters $\Delta = 1$, $\epsilon = 0.3$, and $\omega = \pi/2$ of Fig. 5(c) the peak TVF amplitude is by a factor of about 2 larger than the RBC amplitude. Typically the modulation enhances TVF while it depresses RBC relative to the unmodulated flow. Furthermore, the beginning of vortex growth and the occurrence of the maximum of $\hat{w}(t)$ in a modulation cycle is less delayed relative to the driving for TVF than for RBC. Also the rising slope of $\hat{w}(t)$ just prior to the maximum is steeper in TVF than in RBC. And, finally, for the parameter values of Fig. 5 modulated RBC convection does not show any overshoot and oscillation. All in all the dynamics of the response $\hat{w}(t)$ to a harmonically modulated driving shows less structure in the Rayleigh-Bénard system than in the rotating Couette system.

9. Subharmonic response for large modulation amplitudes

We considered also large amplitudes $\Delta > (2 + \epsilon)/(1 + \epsilon)$ such that the inner cylinder not only reverses its rotation direction during part of the modulation cycle but the driving becomes supercritical for the reversed rotation. Under such conditions we found in the numerical simulation as well as in the model that two types of Taylor vortex flows are generated during a modulation cycle: An intensive one with large amplitudes appearing basically when $\epsilon(t)$ is large and positive and a weaker one basically appearing when $\epsilon(t) < -2$, i.e., when the inner cylinder supercritically rotates in the opposite direction. The flow directions of these two different vortex types can be the same or can be opposite to each other depending on the modulation parameters. Furthermore, the response $w(t)$ can be harmonic or subharmonic.

To illustrate these flow types we show in Fig. 9 $w(t)$ for three representative modulation amplitudes over two periods of the driving obtained from our numerical simulation. In each case $\epsilon = 0$ and $\omega = \pi$. For $\Delta = 2.5$ [Fig. 9(a)] the response is harmonic. Note that TVF with reversed rotation direction grows during the counterrotating phase of the driving when $\epsilon(t) < -2$. Its intensity, however, is very small (the inset is magnified by a factor of 20).

For $\Delta = 2.675$ [Fig. 9(b)] the flow is subharmonic. There fully developed vortices appear with rotation directions alternating from one cycle to the other. In addition to the high-intensity vortices that are generated when $\epsilon(t)$ is large and positive there grow low-intensity vortices when $\epsilon(t) < -2$. Also they reverse their turning direction from one driving period to the other.

For larger modulation amplitudes, e.g., $\Delta = 2.8$ [Fig. 9(c)] the flow is again harmonic with the same periodicity as the driving. Now, however, the low-intensity vortices appearing when the inner cylinder counterrotates supercritically have the same rotation direction as the high-intensity vortices.

In Fig. 10 we show the squared amplitudes $\overline{w^2(t)}$ averaged over two successive periods for $\omega = \pi$, $\epsilon = 0$, and
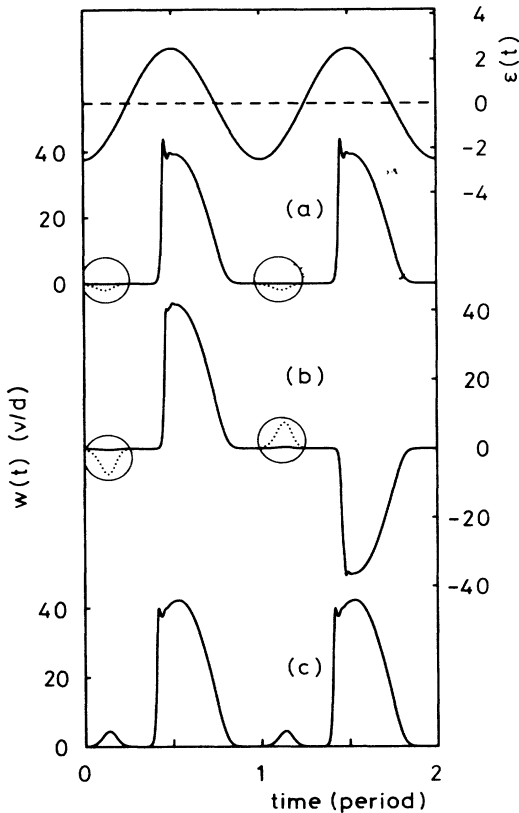
FIG. 9. Response of TVF to harmonic modulation of the driving with large amplitude (a) $\Delta=2.5$, (b) 2.675, and (c) 2.8 for $\epsilon=0$, $\omega=\pi$. The axial velocity $w(t)$ (units of v/d) obtained in our numerical simulation at a fixed position is plotted as a function of time over two periods of the driving $\epsilon(t)$. The latter is shown in the upper part for $\Delta=2.5$. The dotted curves inside the circles represent a magnification of the full curves by a factor of 20.

large modulation amplitudes Δ. The solid line represents our numerical simulation and the dots result from the Galerkin model. In each case subharmonic response is realized for modulation amplitudes Δ between the downwards spikes of the two respective curves. In the transition region of the downwards spikes between harmonic and subharmonic response the TVF flow seems to be complicated. In our Galerkin model we have found additional period doublings and nonperiodic behavior in a very small parameter range. But this problem was not fully investigated. Given the fact that Δ is so large we consider it surprising that the absolute positions of the spikes found in the model agree semiquantitatively (roughly within 10%) with those of our simulation.

C. Mean-squared flow amplitude

In this section we discuss the mean $\overline{w^2(t)}$ of the squared axial flow intensity at the position (r_0,z_0) where in the absence of modulation w becomes maximal (cf. Sec. IV B). In Fig. 11 we show $\overline{w^2(t)}$ as a function of ϵ for
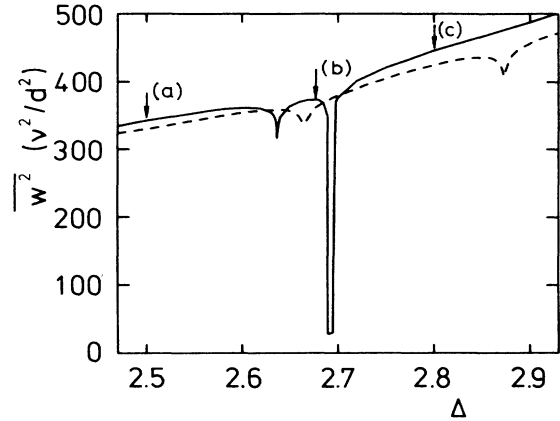

FIG. 10. Mean-squared flow amplitudes averaged over two successive periods, for large modulation amplitude Δ. The solid line represents the numerical simulation and the dashed line results from our Galerkin model for $\omega=\pi$, $\epsilon=0$. In each case subharmonic response [cf. Fig. 9(b)] occurs between the downwards spikes. Arrows indicate Δ values for which $w(t)$ is shown in Fig. 9.

$\Delta=0.3$ and 1 in comparison with the squared flow amplitude in the absence of modulation, $\Delta=0$. Note the perfect agreement between Galerkin model (lines) and simulation (pluses) in the driving and modulation range covered by Fig. 11. Note furthermore that the modulation-induced enhancement of the flow intensity $\overline{w^2(t)}$ relative to $\overline{w^2}(\Delta=0)$ is rather small. This is consistent with and partly explains the smallness of the downwards threshold shift for onset of TVF under small-amplitude modulation of the driving.

The slope $S(\epsilon,\Delta)=\partial\overline{w^2(t)}/\partial\epsilon$ in the presence of modulation is slightly larger than the one for $\Delta=0$. For example, for the parameters of Fig. 11 the deviation is $S(\epsilon=0.1, \Delta=0.3)/S(\epsilon=0.1, \Delta=0)-1\simeq0.1$. We also did a Poincaré-Lindstedt expansion[10,34] of the bifurcating solution of the Galerkin model around $\epsilon=\epsilon_c(\Delta)$. For the slope at threshold we found for small Δ
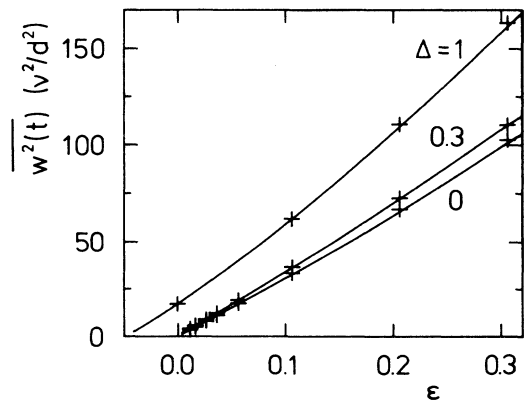

FIG. 11. Mean-squared TVF amplitude $\overline{w^2(t)}$ (in units of v^2/d^2) as a function of ϵ for $\omega=\pi/2$. Solid lines show the result of our model and pluses denote the numerical simulation.

$$S(\epsilon_c,\Delta)=S(0,0)[1+0.57\Delta^2+O(\Delta^4)] \qquad (4.18)$$

for $\eta=0.65$ and $\omega=\pi/2$ with $S(0,0)=285.3$ being the initial slope in the absence of modulation. For still smaller ω there is almost no further variation of S. For $\omega=\pi$ the prefactor of Δ^2 in (4.18) is 0.50 and for $\omega=2\pi$ it is 0.33. Surprisingly, the slope has a strong η dependence. For fixed $\omega(=\pi/2)$, the prefactor of Δ^2 decreases linearly with increasing η. Its value for $\eta=0.75$ is 0.42 and for $\eta=1$ it is 0.01. Since all coefficients of the model, except for ρ_i, are approximately constant in the investigated η range (cf. Table III), this behavior is due to the ρ_i, in particular, to ρ_1.

In Fig. 12 we show in more detail the increase $w^2(t)-w^2(\Delta=0)$ of the squared flow intensity as a function of the square of the modulation amplitude for fixed values of ϵ. Note, first of all, that the modulation-induced flow enhancement increases with the mean rotation rate, i.e., with ϵ as well as with the modulation amplitude. As long as Δ is smaller than $\epsilon/(1+\epsilon)$ $\hat{w}(t)$ oscillates nearly harmonically around its mean and the flow enhancement is proportional to Δ^2. Then, for $\Delta>\epsilon/(1+\epsilon)$ the driving $\epsilon(t)$ becomes partially subcritical during one period and $\hat{w}(t)$ experiences depression during the subcritical driving interval so that the modulation-induced flow enhancement grows slower as a function of Δ^2 there. For still larger Δ the mean-squared flow intensity $\overline{w^2}$ resumes its growth with Δ until at Δ around 2.6 subharmonic response appears with periodically alternating directions of the vortex rotation.

V. SUMMARY AND CONCLUSIONS

We have investigated time-periodic Taylor vortex flow and its bifurcation threshold when the rotation rate of the inner cylinder is modulated with relative amplitude Δ while the outer cylinder is at rest. We have derived a four-mode Galerkin approximation to the axisymmetric Navier-Stokes equations. Therein the radial dependence of the velocity fields is represented in terms of cylindrical Chandrasekhar functions and the axial variation by trigonometric functions. In addition we did finite-difference numerical simulations of the full axisymmetric Navier-Stokes equations using axially periodic boundary conditions.

For both, the stability threshold and the nonlinear modulated TVF the results of these two methods of investigation agree extremely well with each other and also with recent experiments by Ahlers.[8] This agreement between numerical simulation and Galerkin model provides a key to an understanding of the response behavior of TVF to modulated driving: the simulation generates accurate results that serve as a check of the model which in turn provides interpretation and explanation in terms of relatively simple arguments.

Because of complications arising from the formation of a viscous Stokes layer we do not apply our model to modulation periods smaller than about one radial diffusion time d^2/v. The wave number was fixed at the critical one in the absence of modulation, $k_c(\Delta=0)$. Our results follow.
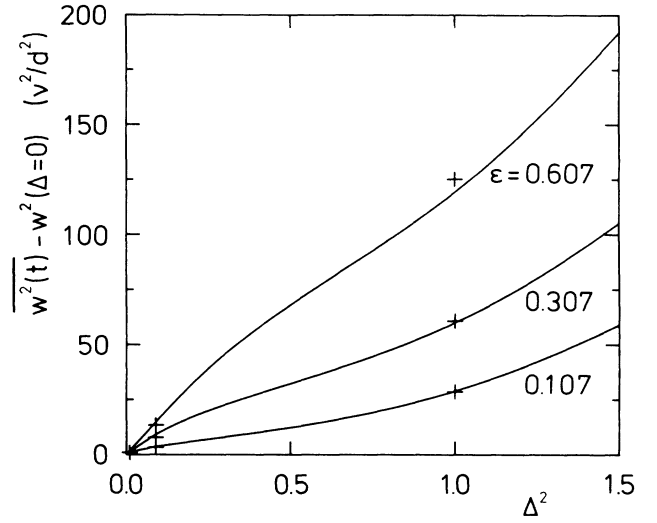
FIG. 12. Modulation-induced enhancement of the squared flow intensity, $\overline{w^2(t)}-w^2(\Delta=0)$ (in units of v^2/d^2), as a function of Δ^2. Parameters and symbols as in Fig. 11.

(1) The velocity fields normalized by their values for the unmodulated case, $\Delta=0$, depend only very weakly on the radius ratio η. Since also $k_c(\Delta)$ varies less than 6% with Δ our results for $\eta=0.65$ and $k=k_c(\Delta=0)$ are generic for $0.5\lesssim\eta\leq 1$ and k near k_c.

(2) The modulation-induced destablization of CCF is small as long as $\Delta\lesssim 1$. For larger Δ the critical Taylor number $T_c(\Delta,\omega)$ for onset of TVF drops off towards zero. Deviations of $T_c(\Delta,\omega)$ from its $\omega\rightarrow 0$ asymptotic value increase $\sim\omega^2$ with the ω variation being weak in the frequency range considered here. Our results for T_c agree very well with the numerical analysis of Riley and Laurence,[3] and for very small Δ with the expansion of Hall.[2] They differ from the analysis of Carmi and Tustaniwskyj.[4,5] The experimentally observed threshold for onset of TVF by Walsh et al.[7] and Ahlers[8] lie by varying amounts (cf. Fig. 4) below our critical values $\hat{T}_c(\Delta,\omega)$. This applies in particular to the low-frequency $(\omega\lesssim 2)$ results of Walsh et al. Possible reasons are finite symmetry-breaking flow disturbances of the ideal CCF basic state.

(3) The smallness of the modulation-induced downwards threshold shift in the limit $(\omega,\Delta)\rightarrow 0$ is the result of two counteracting effects of almost equal size. There is destabilization because modulating the rotation rate like $\Omega(t)/\Omega(\Delta=0)=1+\Delta\cos\omega t$ increases the effective mean Taylor number $\overline{T(t)}/T(\Delta=0)=1+\Delta^2/2$. But there is also the opposite but slightly smaller effect of inertia-induced stabilization[10,34] (of relative magnitude $\simeq 0.45\Delta^2$) so that the net result is a weak destabilization. This analysis is based on the simple limiting behavior of the Galerkin model which can be approximated for $\Delta,\omega\rightarrow 0$ by a parametrically modulated Duffing equation. For larger Δ,ω the response to modulation is more complicated and its description requires the full Galerkin model. In the analogous hydrodynamical problem of convection

in a fluid layer subject to an externally modulated temperature difference it is the latter, i.e., not its square that enters into the field equations and into the Galerkin model equations. Thus in the convective system only the inertia-induced stabilizing effect of modulation is present. The resulting upwards threshold shift for onset of convection is substantially larger than the net destabilization of CCF.

(4) The numerical simulation shows that low-frequency modulation induces in the parameter range investigated here almost no structural changes in the Taylor vortices. The flow varies periodically in a global manner. This response to the harmonic variation of the driving is strongly anharmonic, in particular if the rotation rate $\Omega(t)$ is for a sizable part of the cycle below the static critical threshold, $\Omega_c(\Delta=0)$. Then the TVF amplitude drops to very small values and it takes a long time before TVF grows again to a large amplitude—typically after the maximum of the driving. For large Δ this growth of TVF is very abrupt with a subsequent relaxational oscillation followed by a smooth drop off. A simple generalized amplitude equation does not reproduce this behavior. On the other hand, if $\Omega(t) > \Omega_c(\Delta=0)$ almost all the time then the TVF response is for small ω almost in phase with $\Omega(t)$. In general the dynamics of the response to a harmonically driving shows more structure for TVF than for convective flows for various reasons explained in the text.

(5) With increasing ω the response becomes more and more harmonic and the phase of the peak position of $\hat{w}(t)$ relative to that of the driving increases. Furthermore, phase differences in time between the TVF fields at different radial positions appear.

(6) The mean-squared flow amplitude $\overline{w^2}(t)$ of modulated TVF is enhanced in comparison with the unmodulated driving. Also the slope of $\overline{w^2}(t)$ with respect to Reynolds number is larger at threshold and further up than without modulation.

(7) For such large modulation amplitudes that the driving becomes supercritical with reversed direction, $\Omega(t) < -\Omega_c(\Delta=0)$ during part of the cycle, numerical simulation as well as Galerkin model show subharmonic response of TVF in a narrow band of Δ values. Therein the turning direction of the vortices alternates from one modulation period to the other. The transitions between the two types of limit cycles are complicated and were not investigated thoroughly—in experimental systems it seems likely that Ekman vortices selecting the rotation sense of TVF will suppress its reversion.

ACKNOWLEDGMENTS

APPENDIX A: DERIVATION OF MODEL EQUATIONS

The accuracy of few-mode Galerkin approximations hinges upon a careful selection of the functions representing the flow and the weighting functions for the projection. Fortunately, the spatial structure of nonlinear TVF is very similar to the eigenfunction of the linearized Navier-Stokes equations with the largest eigenvalue. Furthermore, sums over the cylindrical Chandrasekhar functions defined by the simpler eigenvalue problem[14]

$$[(\mathcal{D}\mathcal{D}_*)^2 - \alpha_n^4]|\psi_n(r)\rangle = 0 , \tag{A1a}$$

$$[\mathcal{D}\mathcal{D}_* + \beta_n^2]|v_n(r)\rangle = 0 , \tag{A1b}$$

rapidly converge to the exact radial eigenfunctions of the linear stability problem.

We therefore truncate the expansion of the velocity field for TVF at very low order and make the ansatz (2.8) for ψ and v with $|\psi_1(r)\rangle$ and $|v_n(r)\rangle$ given by (A1). The terms harmonic in z represent TVF and z-independent terms causing nonlinear mode coupling can be seen as modifications of the underlying CCF. We insert the ansatz (2.8) into (2.6) and project[16] Eq. (2.6a) onto

$$\langle \sqrt{2} \cos kz | \langle \psi_1(r) | ,$$

and Eq. (2.6b) onto $\langle \sqrt{2} \sin kz | \langle v_1(r) |$, $\langle v_1(r) |$, and $\langle v_2(r) |$ using the scalar product

$$\langle \phi(z) | \langle f(r) | g(r) \rangle | \psi(z) \rangle$$
$$= \frac{1}{\lambda} \int_0^\lambda dz\, \phi^*(z)\psi(z) \int_{r_1}^{r_2} dr\, r f^*(r) g(r) . \tag{A2}$$

The resulting system of ordinary first-order differential equations for the time-dependent mode amplitudes $\hat{\psi}_{11} \leftrightarrow X$, $\hat{v}_{11} \leftrightarrow Y$, $\hat{v}_{10} \leftrightarrow W$, and $\hat{v}_{20} \leftrightarrow Z$ is given in (2.9). The relation between bare and scaled amplitudes is

$$\hat{\psi}_{11} = \frac{1}{\tau k \langle v_1 | \mathcal{D}_* V_0 | \psi_1 \rangle}$$
$$\times \left[\frac{-\langle v_1 | \mathcal{D}_* V_0 | \psi_1 \rangle^2}{\langle v_2 | \mathcal{D}_{**}(\psi_1 v_1) \rangle \langle v_1 | \psi_1 \mathcal{D}_* v_2 \rangle} \right]^{1/2} X , \tag{A3a}$$

$$\hat{v}_{11} = \left[\frac{-\langle v_1 | \mathcal{D}_* V_0 | \psi_1 \rangle^2}{\langle v_1 | \mathcal{D}_{**}(\psi_1 v_1) \rangle \langle v_1 | \psi_1 \mathcal{D}_* v_2 \rangle} \right]^{1/2} Y , \tag{A3b}$$

$$\hat{v}_{10} = -\frac{\langle v_1 | \mathcal{D}_{**}(\psi_1 v_1) \rangle \langle v_1 | \mathcal{D}_* V_0 | \psi_1 \rangle}{\langle v_2 | \mathcal{D}_{**}(\psi_1 v_1) \rangle \langle v_1 | \psi_1 \mathcal{D}_* v_2 \rangle} W , \tag{A3c}$$

$$\hat{v}_{20} = -\frac{\langle v_1 | \mathcal{D}_* V_0 | \psi_1 \rangle}{\langle v_1 | \psi_1 \mathcal{D}_* v_2 \rangle} Z , \tag{A3d}$$

where $\mathcal{D}_{**} = \mathcal{D}_* + 1/\tau$ and the coefficients in (2.9) are given by

$$\tau(k) = (k^2 + \beta_1^2)^{-1}, \quad b_1(k) = \tau\beta_1^2, \quad b_2(k) = \tau\beta_2^2 , \tag{A4a}$$

$$\sigma(k) = \tau \langle \psi_1 | (\mathcal{D}\mathcal{D}_* - k^2)^2 | \psi_1 \rangle / \langle \psi_1 | k^2 - \mathcal{D}\mathcal{D}_* | \psi_1 \rangle , \tag{A4b}$$

$$\rho_1 = -\frac{\langle \psi_1 | 1/r | v_1^2 \rangle \langle v_1 | \mathcal{D}_{**}(\psi_1 v_1) \rangle \langle v_1 | \mathcal{D}_* V_0 | \psi_1 \rangle}{\langle \psi_1 | V_0/r | v_1 \rangle \langle v_2 | \mathcal{D}_{**}(\psi_1 v_1) \rangle \langle v_1 | \psi_1 \mathcal{D}_* v_2 \rangle} , \tag{A4c}$$

$$\rho_2 = -\frac{\langle \psi_1 | 1/r | v_1 v_2 \rangle \langle v_1 | \mathcal{D}_* V_0 | \psi_1 \rangle}{\langle \psi_1 | V_0 / r | v_1 \rangle \langle v_1 | \psi_1 \mathcal{D}_* v_2 \rangle} \quad , \tag{A4d}$$

$$\rho_3 = -\frac{\langle v_1 | \psi_1 \mathcal{D}_* v_1 \rangle \langle v_1 | \mathcal{D}_{**} (\psi_1 v_1) \rangle}{\langle v_1 | \psi_1 \mathcal{D}_* v_2 \rangle \langle v_2 | \mathcal{D}_{**} (\psi_1 v_1) \rangle} \quad , \tag{A4e}$$

$$p(t) = 1 + \Delta \frac{\langle \psi_1 | V_1 / r | v_1 \rangle}{\langle \psi_1 | V_0 / r | v_1 \rangle} \quad , \tag{A4f}$$

$$q(t) = 1 + \Delta \frac{\langle \psi_1 | \mathcal{D}_* V_1 | v_1 \rangle}{\langle \psi_1 | \mathcal{D}_* V_0 | v_1 \rangle} \quad . \tag{A4g}$$

Furthermore, the quotient

$$\frac{\hat{\tau}}{s(k)} = \frac{T/T_c(\Delta=0)}{T_{SB}(k, \Delta=0)/T_c(\Delta=0)} \tag{A4h}$$

enters, i.e., the Taylor number reduced by the stability boundary

$$T_{SB}(k, \Delta=0) = -\frac{1-\eta}{\eta} \frac{(\beta_1^2 + k^2) \langle \psi_1 | (\mathcal{D}\mathcal{D}_* - k^2)^2 | \psi_1 \rangle}{2k^2 \langle \psi_1 | V_0 / r | v_1 \rangle \langle v_1 | \mathcal{D}_* V_0 | \psi_1 \rangle} \tag{A4i}$$

in the absence of modulation. Here $s(k)$ is the neutral curve normalized by its critical value, $T_c(\Delta=0)$.

For an application of the model (2.9) all coefficients and scaling factors have to be computed. The general case of a wide gap requires an evaluation of the solutions of (A1), i.e., of the cylindrical Chandrasekhar functions

$$\psi_1(r) = \mathcal{C}_1(r) = N_1 [J_1(\alpha_1 r) + B_1 Y_1(\alpha_1 r) + C_1 I_1(\alpha_1 r) + D_1 K_1(\alpha_1 r)] \quad , \tag{A5a}$$

$$v_n(r) = \mathcal{E}_n(r) = M_n [J_1(\beta_n r) + \tilde{B}_n Y_1(\beta_n r)], \quad n = 1, 2 . \tag{A5b}$$

TABLE III. Constants and scaling factors for the model equations (2.9) for some radius ratios η. Data have been evaluated for $k = k_c(\eta, \Delta=0)$.

	η			
	0.5	0.65	0.8	1
k_c	3.119	3.106	3.100	3.098
T_c	4786	3101	2293	1728
b_1	0.512	0.509	0.508	0.507
b_2	1.998	2.016	2.025	2.028
ρ_1	-0.084	-0.058	-0.033	0
ρ_2	-0.048	-0.032	-0.018	0
ρ_3	0.023	0.009	0.003	0
σ	1.904	1.928	1.940	1.944
τ	0.050	0.051	0.051	0.051
α_1	4.750	4.738	4.732	4.730
β_1	3.197	3.163	3.148	π
β_2	6.312	6.294	6.286	2π
$\hat{\psi}_{11}/X$	-0.761	-0.664	-0.523	-1.232
$\hat{v}_{11}/Y$	0.078	0.082	0.073	0.1934
$\hat{v}_{20}/Z$	-0.080	-0.082	-0.073	0.1934
$\hat{v}_{10}/W$	-0.017	-0.011	-0.005	0

They are superpositions of first order Bessel functions.[14] The constants N_1, B_1, C_1, D_1, M_n, and $\tilde{B}_n$ and the characteristic roots α_1 and β_n are determined by boundary normalization, and solvability conditions.

We used these cylindrical Chandrasekhar functions in evaluating the scalar products (A2). As a reference we give all time-independent coefficients and critical values in Table III. The time-dependent factors $p(t)$ [Eq. (A4f)] and $q(t)$ [Eq. (A4g)] have the form

$$p(t) = 1 + \Delta A_p \cos(\omega t - \varphi_p) \quad , \tag{A6a}$$

$$q(t) = 1 + \Delta A_q \cos(\omega t - \varphi_q) \quad . \tag{A6b}$$

$A_p = A_q = 1$ and $\varphi_p = \varphi_q = 0$ for $\omega \to 0$. Since $p(t)$ and $q(t)$ are practically independent of η we have listed A_p, A_q, φ_p, and φ_q in Table IV for $\eta = 0.65$ and several modulation frequencies ω.

Since the calculation of the coefficients entering our model with the cylindrical Chandrasekhar functions is rather involved, a further approximation may be useful. In the narrow-gap limit ($\eta \to 1$) the radial eigenfunctions $|\psi_1(r)\rangle$ and $|v_n(r)\rangle$ are plane Chandrasekhar functions,[14] $C_1(r)$ and $E_n(r)$, respectively (see Appendix B). Especially for small gaps the plane Chandrasekhar functions $C_1(r)$ and $E_n(r)$ do not deviate much from the cylindrical ones, $\mathcal{C}_1(r)$ and $\mathcal{E}_n(r)$. With the replacement (B2)

$$\mathcal{C}_1(r) \simeq (1-\eta)^{-1/2} C_1(x) \quad ,$$
$$\mathcal{E}_n(r) \simeq (1-\eta)^{-1/2} E_n(x) \quad , \tag{A7}$$

and $r = x + \frac{1}{2}(1+\eta)/(1-\eta)$ the integrals appearing in the model's coefficients as well as the basic modes can be calculated analytically. The squared deviation

$$\alpha := \int_{r_1}^{r_2} [\mathcal{C}_1(r) - \sqrt{1-\eta} C_1(x)]^2 r \, dr$$

can be considered to measure the quality of this approximation. For $\eta > 0.5$ we get $\alpha < 0.02$ and for $\eta > 0.65$ even $\alpha < 0.01$. Because of this similarity of $\mathcal{C}_1(r)$ and $C_1(x)$ it is the factor $\sqrt{1-\eta}$ relating both function systems that determines the overall dependence on η of all static properties of the model in the considered η range. For example, the critical Taylor number $T_c(\Delta=0)$ (A4i) varies with η as $T_c(\Delta=0, \eta)/T_c(\Delta=0, \eta=1) \sim 1/\eta$. In a similar way the approximate η dependence of the other coefficients can be found.

APPENDIX B: ANALOGY TO LORENZ MODEL FOR CONVECTION

Similarities between the Taylor-Couette and the Rayleigh-Bénard problem are most pronounced in the

TABLE IV. Frequency dependence of time-dependent coefficients $p(t)$ and $q(t)$ for the model for $\eta = 0.65$.

ω	A_p	A_q	φ_p	φ_q
$\to 0$	1	1	0	0
$\pi/2$	0.988	1.002	0.168	0.025
π	0.954	1.008	0.329	0.053
2π	0.847	1.023	0.610	0.120

limit of a narrow gap. For a discussion of the case $\eta \to 1$ or $\delta = d/R_1 = (1-\eta)/\eta \to 0$, we expand Eqs. (2.6) to lowest order $O(\delta^0)$. The relevant Taylor number is $T = (R_1 \Omega d/v)^2 \delta$. Defining the radial coordinate

$$x = r - \frac{1}{2} \frac{1+\eta}{1-\eta} \in [-\tfrac{1}{2}, \tfrac{1}{2}] \qquad (B1)$$

the basic CCF for $\Delta = 0$ is $V_0(x) = \frac{1}{2} - x$. Because of the Cartesian geometry arising for $\delta \to 0$ we expand the radial dependence of the TVF fields in terms of plane Chandrasekhar functions[14]

$$\psi_1(r) = C_1(x) = \frac{\cosh(\lambda_1 x)}{\cosh(\lambda_1/2)} - \frac{\cos(\lambda_1 x)}{\cos(\lambda_1/2)} ,$$

$$\lambda_1 = 4.730\,04 \qquad (B2a)$$

$$v_1(r) = E_1(x) = \sqrt{2} \cos\pi x ,$$

$$v_2(r) = E_2(x) = \sqrt{2} \sin 2\pi x . \qquad (B2b)$$

They are eigenfunctions of ∂_x^4 and ∂_x^2 satisfying rigid boundary conditions $v = \psi = \partial_x \psi = 0$ at $x = \pm \frac{1}{2}$. The coefficients of the model are then evaluated with the radial scalar product $\langle f(x) | g(x) \rangle = \int_{-1/2}^{1/2} f^* g \, dx$. Due to the symmetries of $C_1(x)$ and $E_n(x)$ all coefficients ρ_i [Eqs. (A4c)–(A4e)] and the scaling factor of W [Eq. (A3c)] vanish. Thus the model (2.9) reduces in the narrow-gap limit to

$$\frac{\tau}{\sigma} \dot{X} = -[X - p(t)\tilde{Y}] , \qquad (B3a)$$

$$\tau \dot{\tilde{Y}} = -\tilde{Y} + X[(\hat{r}/s)q(t) - \tilde{Z}] , \qquad (B3b)$$

$$\tau \dot{\tilde{Z}} = -b_2 \tilde{Z} + X\tilde{Y} , \qquad (B3c)$$

with $\tilde{Y} = Y\hat{r}/s$ and $\tilde{Z} = Z\hat{r}/s$.

For stationary driving ($p = q = 1$) Eqs. (B3) are identical to a Lorenz model[44] for convection in a fluid of unit Prandtl number provided $\hat{r}/s$ in (B3b) is replaced by the reduced Rayleigh number. The convective model was derived by Niederländer[44] for rigid horizontal boundary conditions using Chandrasekhar functions. The coefficients $\tau = 0.051$, $\sigma = 1.944$, and $b_2 = 2.028$ (cf. Table III) are the same in both models. The structural similarity of the models for flow in the form of vortex rolls in the Couette-Taylor system and the Rayleigh-Bénard system is not surprising since for $\eta \to 1$ the curved geometry of the former system approaches the planar one of the latter. Moreover, also for η in the range $\frac{1}{2} < \eta < 1$ the statics and dynamics of the unmodulated ($p = q = 1$) TVF model (2.9) are very similar to those of (B3) and with it to those of the unmodulated convective Lorenz model. The reason is that the size of the coefficients ρ_i in (2.9) are small, $|\rho_i| < 0.1$, and that b_2, σ, and τ vary less than 3% in the range $\frac{1}{2} < \eta < 1$.

Note, however, the differences that are present even in the case of stationary driving: Into the variables $\tilde{Y}$ and $\tilde{Z}$ enters the control parameter $\hat{r}$. Furthermore, and more important, the driving force couples differently to the variables in the two models. In the Taylor-Couette system the square of the inner cylinder's rotation velocity, i.e., the squared Reynolds number enters via $\hat{r}$ whereas in the Rayleigh-Bénard system it is the Rayleigh number, i.e., the temperature stress itself that enters the model equations as the control parameter.

If the driving force is modulated in time there arise additional and far more consequential differences that may be seen by comparing (B3) with the corresponding equations for modulated convection.[10,44] Loosely speaking in the convective model $p(t) = 1$ and only $q(t)$ reflects the time dependence of the driving whereas for modulated TVF the modulated driving enters via $p(t)$ and $q(t)$. The resulting differences in the stability properties of the basic state and in the response of the secondary flow are discussed in Secs. IV A 6 and IV B 8, respectively.

[1]R. J. Donnelly, F. Reif, and H. Suhl, Phys. Rev. Lett. **9**, 363 (1962); R. J. Donnelly, Proc. Roy. Soc. London, Ser. A **281**, 130 (1964).

[2]P. Hall, J. Fluid Mech. **67**, 29 (1975).

[3]P. J. Riley and R. L. Laurence, J. Fluid Mech. **75**, 625 (1976).

[4]S. Carmi and J. I. Tustaniwskyj, J. Fluid Mech. **108**, 19 (1981).

[5]J. I. Tustaniwskyj and S. Carmi, Phys. Fluids **23**, 1732 (1980).

[6]R. Thompson, Ph.D. thesis, Massachusetts Institute of Technology, 1968.

[7]T. J. Walsh, W. T. Wagner, and R. J. Donnelly, Phys. Rev. Lett. **58**, 2543 (1987); T. J. Walsh, Ph.D. thesis, University of Oregon, 1988.

[8]G. Ahlers, Bull. Am. Phys. Soc. **32**, 2068 (1987); (private communication).

[9]T. J. Walsh and R. J. Donnelly, Phys. Rev. Lett. **60**, 700 (1988).

[10]G. Ahlers, P. C. Hohenberg, and M. Lücke, Phys. Rev. A **32**, 3493 (1985).

[11]G. Ahlers, P. C. Hohenberg, and M. Lücke, Phys. Rev. A **32**, 3519 (1985).

[12]E. N. Lorenz, J. Atmos. Sci. **20**, 130 (1963).

[13]R. C. DiPrima, P. M. Eagles, and B. S. Ng, Phys. Fluids **27**, 2403 (1984).

[14]S. Chandrasekhar, *Hydrodynamic and Hydromagnetic Stability* (Clarendon, Oxford, 1961).

[15]D. Y. Hsieh and F. Chen, Phys. Fluids **27**, 321 (1984).

[16]F. Chen and D. Y. Hsieh (unpublished).

[17]G. Z. Gershuni and E. M. Zhukhovitskii, *Convective Stability of Incompressible Fluids* (Keter, Jerusalem, 1976).

[18]D. Roth, Diploma thesis, Universität Saarbrücken, 1988.

[19]M. Lücke, M. Mihelcic, and K. Wingerath, Phys. Rev. A **31**, 396 (1985). There is a misprint in Eq. (A2c) of this reference: $\partial_w u$ should read $\partial_z u$.

[20]J. E. Welch, F. H. Harlow, J. P. Shannon, and B. J. Daly, Los Alamos Scientific Laboratory Report No. LA-3425, 1966 (unpublished).

[21]W. Barten, Diploma thesis, Universität Saarbrücken, 1986.

[22]C. W. Hirt, B. D. Nichols, and N. C. Romero, Los Alamos Scientific Laboratory Report No. LA-5652, 1975 (unpublished).

[23]A. J. Chorin, Math. Comp. **22**, 745 (1968).

[24]M. A. Dominguez-Lerma, G. Ahlers, and D. S. Cannell, Phys. Fluids **27**, 856 (1984).

[25]P. H. Roberts in Appendix of R. J. Donnelly and K. W. Schwarz, Proc. Roy. Soc. London, Ser. A **283**, 531 (1965).

[26]A. Davey, J. Fluid Mech. **14**, 336 (1962).

[27]G. Ahlers, D. S. Cannell, M. A. Dominguez-Lerma, and R. Heinrichs, Physica **23D**, 202 (1986); R. M. Heinrichs, D. S. Cannell, G. Ahlers, and M. Jefferson, Phys. Fluids **31**, 250 (1988); T. Berland, T. Jøssang, and J. Feder, Phys. Scr. **34**, 421 (1986).

[28]M. Lücke (unpublished).

[29]J. K. Bhattacharjee, K. Banerjee, and K. Kumar, J. Phys. A **L19**, 835 (1986).

[30]H. Kuhlmann, Ph. D. thesis, Universität Saarbrücken, 1986.

[31]H. Kuhlmann, Phys. Rev. A **32**, 1703 (1985).

[32]K. Kumar, J. K. Bhattacharjee, and K. Banerjee, Phys. Rev. A **34**, 5000 (1986).

[33]T. J. Walsh, Ph.D. thesis, University of Orgeon, 1988.

[34]M. Lücke and F. Schank, Phys. Rev. Lett. **54**, 1465 (1985); M. Lücke, in *Noise in Nonlinear Dynamical Systems,* edited by F. Moss and P. V. E. McClintock (Cambridge University Press, Cambridge, 1988), Vol. 2.

[35]M. A. Dominguez-Lerma, Ph.D. thesis, Santa Barbara, 1986.

[36]G. P. Neitzel, J. Fluid. Mech. **141**, 51 (1984).

[37]E. R. Cooper, D. F. Jankowski, G. P. Neitzel, and T. H. Squire, J. Fluid Mech. **161**, 97 (1985).

[38]K. Takeyama, Prog. Theor. Phys. **63**, 91 (1980).

[39]D. S. Cannell, M. A. Dominguez-Lerma, and G. Ahlers, Phys. Rev. Lett. **50**, 1365 (1983).

[40]G. Ahlers and D. S. Cannell, Phys. Rev. Lett. **50**, 1583 (1983).

[41]M. Lücke, M. Mihelcic, B. Kowalski, and K. Wingerath, in *The Physics of Structure Formation: Theory and Simulation,* edited by W. Güttinger and G. Dangelmayr (Springer, Berlin, 1987).

[42]B. Jhaveri and G. M. Homsy, J. Fluid. Mech. **98**, 329 (1980); **114**, 251 (1982).

[43]C. Meyer, G. Ahlers, and D. S. Cannell, Phys. Rev. Lett. **59**, 1577 (1987).

[44]J. Niederländer, Diploma thesis, Universität Saarbrücken, 1986.